Linear temporal and spatio-temporal stability analysis of a binary liquid film flowing down an inclined uniformly heated plate

JUN HU[1], HAMDA BEN HADID[2], DANIEL HENRY[2] AND ABDELKADER MOJTABI[3]

[1]Institute of Applied Physics and Computational Mathematics, Beijing 100088, China
hu_jun@iapcm.ac.cn

[2]Laboratoire de Mécanique des Fluides et d'Acoustique, CNRS/Université de Lyon,
Ecole Centrale de Lyon/Université Lyon 1/INSA de Lyon,
ECL, 36 avenue Guy de Collongue, 69134 Ecully Cedex, France

[3]IMFT, UMR CNRS/INP/UPS 5502, UFR MIG, Université Paul Sabatier, 118 route de Narbonne,
31062 Toulouse Cedex, France

Temporal and spatio-temporal instabilities of binary liquid films flowing down an inclined uniformly heated plate with Soret effect are investigated by using the Chebyshev collocation method to solve the full system of linear stability equations. Seven dimensionless parameters, i.e. the Kapitza, Galileo, Prandtl, Lewis, Soret, Marangoni, and Biot numbers (Ka, G, Pr, L, χ, M, B), as well as the inclination angle (β) are used to control the flow system. In the case of pure spanwise perturbations, thermocapillary S- and P-modes are obtained. It is found that the most dangerous modes are stationary for positive Soret numbers ($\chi \geqslant 0$), and oscillatory for $\chi < 0$. Moreover, the P-mode which is short-wave unstable for $\chi = 0$ remains so for $\chi < 0$, but becomes long-wave unstable for $\chi > 0$ and even merges with the long-wave S-mode. In the case of streamwise perturbations, a long-wave surface mode (H-mode) is also obtained. From the neutral curves, it is found that larger Soret numbers make the film flow more unstable as do larger Marangoni numbers. The increase of these parameters leads to the merging of the long-wave H- and S-modes, making the situation long-wave unstable for any Galileo number. It also strongly influences the short-wave P-mode which becomes the most critical for large enough Galileo numbers. Furthermore, from the boundary curves between absolute and convective instabilities (AI/CI) calculated for both the long-wave instability (S- and H-modes) and the short-wave instability (P-mode), it is shown that for small Galileo numbers the AI/CI boundary curves are determined by the long-wave instability, while for large Galileo numbers they are determined by the short-wave instability.

1. Introduction

A liquid film flowing down an inclined plate is a typical model of simple open flows, which not only has widespread engineering applications in materials processing, biomedical engineering, food and chemical industries, but also is of a significant interest in fundamental problems, such as the formation of surface waves, the breaking of a stream into rivulets, and the transition from laminar shear flow to complex turbulence. Since the pioneering experiment of Kapitza & Kapitza (1949),

the mechanisms of the film instability have been extensively studied for isothermal and heated films by theoretical linear and nonlinear approaches. Benjamin (1957) and Yih (1963) first performed a linear stability analysis of isothermal falling films and identified the surface wave instability through a long-wave asymptotic approach. Lin (1969), Gjevik (1970) and Pumir, Manneville & Pomeau (1983) then performed weakly nonlinear analyses based on long-wave evolution equations. Pumir *et al.* (1983) obtained subcritical instabilities with their model, but this result was later shown as non-physical and due to the high nonlinearity of the inertia term in the Benney equation (Ooshida 1999; Oron & Gottlieb 2002; Scheid *et al.* 2005). It is now well known that the primary instability in the isothermal film flow is always supercritical (Thiele & Knobloch 2004). A detailed discussion on the results obtained for an isothermal film flow can be found in the review papers of Chang (1994) and Oron, Davis & Bankoff (1997) and in the references therein.

The absolute/convective instability for isothermal falling films has been intensively studied by Brevdo *et al.* (1999). Because the model equations such as the Benney equation (Benney 1966) and the integral boundary layer equation derived by Shkadov (1967) were generally valid for limited regions of the parameter space, they used the full linearized Navier–Stokes equations to investigate the characteristics of the absolute/convective instability through the exact Briggs–Bers collision criterion. They explored a large region of the parameter space and pointed out that the isothermal film flow is convectively unstable, which agrees with all experiments. Considering the convective property of such open flows, Brevdo *et al.* further studied the properties of the spatially amplifying waves and found results in complete agreement with the experiments performed by Liu, Paul & Gollub (1993). Later, by using weighted-residual approximations (Ruyer-Quil & Manneville 2000), Ruyer-Quil & Manneville (2002) predicted the properties of the wave packets at the linear stage and found results in excellent agreement with the exact results of Brevdo *et al.* (1999) in a wide range of Reynolds numbers.

Falling films along a uniformly heated inclined plate are not only susceptible to the surface wave instability (H-mode) but also to two types of thermocapillary instability (S- and P-modes) which have already been identified for purely spanwise and streamwise perturbations by Goussis & Kelly (1990); Goussis & Kelly (1991). A temporal stability analysis of these modes shows that the mechanisms of triggering of S- and H-modes are respectively associated with the thermocapillary forces induced by the modification of the basic temperature at the free surface by the surface deformation and with the shear stress of the basic flow at the deformed free surface. The two modes, which both require a deformable free surface, reinforce each other and are stabilized by the hydrostatic pressure and the surface tension. Since the latter force is more effective for the short-wavelength disturbances, the instability due to the two modes takes the form of long waves. The P-mode of thermocapillary instability is caused by the interaction of the basic temperature with the perturbation velocity field, and a deformable free surface is not required in this case. When the heated film is horizontal, the thermocapillary instabilities still can be observed as they do not need a mean flow. The long-wave thermocapillary instability induced by the S-mode was first found by Scriven & Sternling (1964). The study was later extended by Smith (1966) to include the effect of gravity. The P-mode of instability was first mentioned by Pearson (1958).

In the case of a binary liquid layer with a free surface, the thermocapillary forces can be produced by the dependence of the surface tension on both the temperature and the solute concentration. Therefore the thermocapillary instability may appear

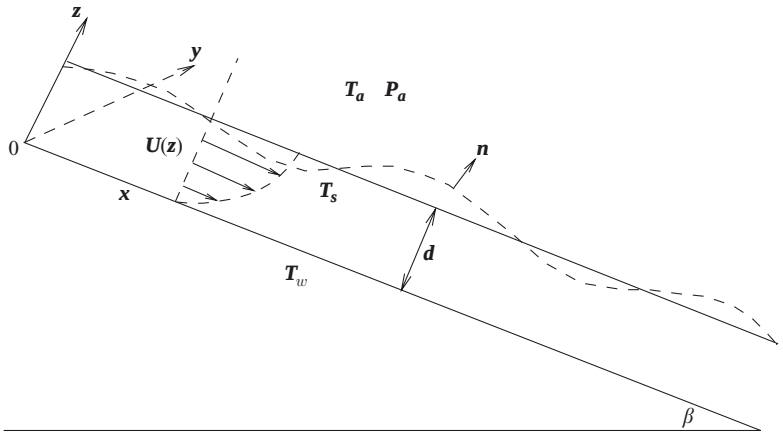

FIGURE 1. Schematic representation of a binary liquid film flowing down an inclined uniformly heated plate.

due to solutal effects induced by the Soret effect. For such a binary fluid, many studies have been performed in the horizontal situation, starting with the precursor work of Takashima (1979) who extended Pearson's linear stability analysis to binary mixtures, thus showing the influence of the Soret effect on the P-mode. Joo (1995) considered a model with a deformable free surface and showed the influence of this effect on the instability thresholds in a binary layer with Soret effect, heated from above or below. His model generally does not include the hydrostatic effect. Among the recent studies, we mention the work of Podolny, Oron & Nepomnyashchy (2005, 2006) who extensively studied the influence of the Soret effect on the S-mode, in a situation where it is the heat flux which is imposed across the layer. Temporal and spatio-temporal stability analyses of the uniformly heated falling film with Soret effect have, however, not yet been performed. This is the subject of this paper. In § 2, the physical model is described and the three-dimensional linear stability equations are derived. In § 3, the neutral curves for both spanwise and streamwise perturbations are plotted and they allow characterization of the temporal stability of the falling film with Soret effect. In § 4, the spatio-temporal instabilities are investigated through the study of their local growth rate in a moving frame. The boundary curves between absolute and convective instabilities are then plotted and analysed in the (M, G)-plane. We finally summarize the findings of the paper in § 5.

2. Formulation of the physical model

We consider a binary liquid film with an average thickness d flowing down a uniformly heated plate inclined at an angle β to the horizontal under the effect of gravity, as shown in figure 1. The ambient gas is assumed motionless with constant temperature T_a and pressure P_a, and the plate is maintained at a constant temperature T_w. At the free surface, the surface tension is assumed to be linearly dependent on both the temperature T and the solute concentration C. This can be expressed by

$$\sigma = \sigma_0 - \sigma_t(T - T_a) + \sigma_c(C - C_0), \tag{2.1}$$

where C_0 is the concentration induced at the plate by the Soret effect in the diffusive state, and σ_0 is the value of the surface tension at T_a and C_0; $\sigma_t = -\partial\sigma/\partial T$ and

$\sigma_c = \partial\sigma/\partial C$ are constant parameters which are positive for most common binary mixtures.

In the classical Fourier and Fick laws, the heat and mass fluxes are taken proportional to the temperature and concentration gradients respectively. In fact, both fluxes should be linear combinations of the two gradients (de Groot & Mazur 1969). The contribution of the temperature gradient to the mass flux is called the Soret effect, while the contribution of the concentration gradient to the heat flux is called the Dufour effect. The Dufour effect, however, is exceedingly weak in liquids and can be safely neglected, while the Soret effect can be significant and will be taken into account hereafter. Therefore, in what follows, the heat flux J_h and mass flux J_m are given by

$$J_h = -k_{th}\nabla T, \quad J_m = -\rho D(\nabla C + \alpha\nabla T), \tag{2.2}$$

where ρ, k_{th}, D and α are the density, the thermal conductivity, the mass diffusivity, and the Soret coefficient of the binary mixture, respectively.

The three-dimensional equations governing the binary fluid flow in the thin film along the plate (in the presence of the Soret effect, but without consideration of the buoyancy effect) are given by

$$\nabla\cdot\boldsymbol{U} = 0, \tag{2.3a}$$

$$\frac{\mathrm{d}\boldsymbol{U}}{\mathrm{d}t} = -\rho^{-1}\nabla P + \nu\nabla^2\boldsymbol{U} + \boldsymbol{g}, \tag{2.3b}$$

$$\frac{\mathrm{d}T}{\mathrm{d}t} = \kappa\nabla^2 T, \tag{2.3c}$$

$$\frac{\mathrm{d}C}{\mathrm{d}t} = D\nabla^2 C + \alpha D\nabla^2 T. \tag{2.3d}$$

Here, $\nabla = (\partial_x, \partial_y, \partial_z)$, $\boldsymbol{U} = (U, V, W)$ and $\boldsymbol{g} = (g\sin\beta, 0, -g\cos\beta)$ are vectors of the gradient operator, fluid velocity and gravity acceleration, P is the fluid pressure, ν and κ are the kinematic viscosity and the thermal diffusivity of the binary mixture.

The boundary conditions at the bottom rigid surface $z = 0$ express the no-slip condition for the velocities, the prescribed conductive temperature and the mass impermeability, respectively:

$$\boldsymbol{U} = 0, \quad T = T_w, \quad \partial_z C + \alpha\partial_z T = 0. \tag{2.4}$$

At the free surface $z = H(x, y, t)$ the boundary conditions are, respectively, the kinematic boundary condition, the dynamic boundary condition, the heat transfer governed by the Newton law of cooling and the mass impermeability:

$$H_t + UH_x + VH_y = W, \tag{2.5a}$$

$$\boldsymbol{T}\cdot\boldsymbol{n} = -P_a\boldsymbol{n} + 2H_c\sigma\boldsymbol{n} + \nabla_s\sigma, \tag{2.5b}$$

$$\boldsymbol{n}\cdot k_{th}\nabla T + q(T - T_a) = 0, \tag{2.5c}$$

$$\boldsymbol{n}\cdot k_{th}\nabla C - \alpha q(T - T_a) = 0, \tag{2.5d}$$

where ∇_s is the gradient vector in the tangent plane at the interface and where the stress tensor $\boldsymbol{T}$ and mean curvature H_c are given by

$$\boldsymbol{T} = -P\boldsymbol{I} + \mu(\nabla\boldsymbol{U} + (\nabla\boldsymbol{U})^{\mathrm{T}}),$$

$$2H_c = -\nabla\cdot\boldsymbol{n};$$

$\boldsymbol{n}$ is the unit outward vector normal to the interface, μ is the dynamical viscosity of the binary mixture, q is the heat transfer coefficient describing the rate of heat transfer from the liquid to the ambient gas phase at the constant temperature T_a.

Without disturbance of the flat free surface, the basic parallel flow is the same as for the isothermal film. The basic solution can thus be represented by

$$U(z) = \frac{\rho g d^2 \sin\beta}{2\mu}\left[2\frac{z}{d} - \left(\frac{z}{d}\right)^2\right], \tag{2.6a}$$

$$T(z) = T_w - \frac{q(T_w - T_a)}{k + qd}z, \tag{2.6b}$$

$$C(z) = C_0 + \frac{\alpha q(T_w - T_a)}{k + qd}z. \tag{2.6c}$$

The dimensionless variables of the problem are defined through the transformations

$$t \to \frac{d^2}{\nu}t, \quad [x, y, z, H] \to d[x, y, z, h], \tag{2.7a}$$

$$\boldsymbol{U}(U, V, W) \to \frac{\nu}{d}\boldsymbol{u}(u, v, w), \quad P \to P_a + \frac{\rho\nu^2}{d^2}p, \tag{2.7b}$$

$$T \to T_a + (T_w - T_a)\theta, \quad C \to C_0 + \frac{\sigma_t}{\sigma_c}(T_w - T_a)c. \tag{2.7c}$$

This yields the dimensionless form of the governing equations

$$\nabla\cdot\boldsymbol{u} = 0, \tag{2.8a}$$

$$\frac{\mathrm{d}\boldsymbol{u}}{\mathrm{d}t} = -\nabla p + \nabla^2\boldsymbol{u} + \boldsymbol{G}, \tag{2.8b}$$

$$Pr\frac{\mathrm{d}\theta}{\mathrm{d}t} = \nabla^2\theta, \tag{2.8c}$$

$$Sc\frac{\mathrm{d}c}{\mathrm{d}t} = \nabla^2 c + \chi\nabla^2\theta, \tag{2.8d}$$

where $\boldsymbol{G} = (G\sin\beta, 0, -G\cos\beta)$. And the dimensionless boundary conditions are: at the wall $z = 0$,

$$\boldsymbol{u} = 0, \quad \theta = 1, \quad c_z + \chi\theta_z = 0; \tag{2.9}$$

and at the free surface $z = h(x, y, t)$,

$$h_t + uh_x + vh_y = w, \tag{2.10a}$$

$$\boldsymbol{T}\cdot\boldsymbol{n} = 2H_c\Sigma[1 - Ca(\theta - c)]\boldsymbol{n} - \frac{Ma}{Pr}(\nabla_s\theta - \nabla_s c), \tag{2.10b}$$

$$\boldsymbol{n}\cdot\nabla\theta + Bi\theta = 0, \tag{2.10c}$$

$$\boldsymbol{n}\cdot\nabla c - \chi Bi\theta = 0, \tag{2.10d}$$

where the dimensionless stress tensor is $\boldsymbol{T} = -p\boldsymbol{I} + \left(\nabla \boldsymbol{u} + (\nabla \boldsymbol{u})^{\mathrm{T}}\right)$, and the dimensionless parameters of the problem

$$G = \frac{gd^3}{\nu^2}, \quad Pr = \frac{\nu}{\kappa}, \quad Sc = \frac{\nu}{D}, \quad L = \frac{D}{\kappa}, \tag{2.11a}$$

$$\chi = \frac{\alpha \sigma_c}{\sigma_t}, \quad Ma = \frac{\sigma_t (T_w - T_a) d}{\mu \kappa}, \quad Bi = \frac{qd}{k_{th}}, \tag{2.11b}$$

are respectively the Galileo, Prandtl, Schmidt, Lewis, Soret, Marangoni, and Biot numbers, $\Sigma = \sigma_0 d/(\rho \nu^2)$ is the dimensionless surface tension and $Ca = \sigma_t (T_w - T_a)/\sigma_0$ is the capillary number. Obviously, there is a relation $L = Pr/Sc$ between the Lewis, Prandtl, and Schmidt numbers, and another relation $\Sigma Ca = Ma/Pr$ between the dimensionless surface tension and the capillary, Marangoni, and Prandtl numbers. The value of σ_c/σ_t is usually of order 10^2 K, while the value of α ranges between -10^{-2} and 10^{-2}. Therefore, the typical value of χ varies in the range $-1 < \chi < 1$. The Lewis number of a liquid binary mixture is usually small and ranges between 10^{-4} and 10^{-2}. For convenience, we will adopt the Kapitza number Ka, a new Marangoni number M and a new Biot number B in our linear stability computations and analyses (see Appendix A).

The dimensionless basic flow can be expressed as

$$\bar{u}(z) = G \sin(\beta)(z - \tfrac{1}{2} z^2), \tag{2.12a}$$

$$\bar{p}(z) = G \cos(\beta)(1 - z), \tag{2.12b}$$

$$\bar{\theta}(z) = 1 - \frac{Bi}{1 + Bi} z, \tag{2.12c}$$

$$\bar{c}(z) = \frac{Bi \chi}{1 + Bi} z, \tag{2.12d}$$

where $G \sin \beta$ is equivalent to a Reynolds number ($G \sin \beta = Re$). Around the basic state, the disturbed flow can be decomposed as $u = \bar{u} + u'$, $v = v'$, $w = w'$, $p = \bar{p} + p'$, $\theta = \bar{\theta} + \theta'$, $c = \bar{c} + c'$ and $h = 1 + \eta$, and we can obtain the linearized perturbation equations

$$u'_x + v'_y + w'_z = 0, \tag{2.13a}$$

$$u'_t + \bar{u} u'_x + \mathrm{D}\bar{u} w' = -p'_x + \nabla^2 u', \tag{2.13b}$$

$$v'_t + \bar{u} v'_x = -p'_y + \nabla^2 v', \tag{2.13c}$$

$$w'_t + \bar{u} w'_x = -p'_z + \nabla^2 w', \tag{2.13d}$$

$$Pr(\theta'_t + \bar{u} \theta'_x + \mathrm{D}\bar{\theta} w') = \nabla^2 \theta', \tag{2.13e}$$

$$Sc(c'_t + \bar{u} c'_x + \mathrm{D}\bar{c} w') = \nabla^2 c' + \chi \nabla^2 \theta', \tag{2.13f}$$

and linearized boundary conditions

$$z=0: \qquad u'=v'=w'=\theta'=0, \tag{2.14a}$$

$$z=0: \qquad c'_z+\chi\theta'_z=0, \tag{2.14b}$$

$$z=1: \qquad \eta_t+\bar{u}\eta_x-w'=0, \tag{2.14c}$$

$$z=1: \qquad u'_z+w'_x+(\mathrm{D}^2\bar{u})\eta+(Ma/Pr)(\theta'_x+\mathrm{D}\bar{\theta}\eta_x-c'_x-\mathrm{D}\bar{c}\eta_x)=0, \tag{2.14d}$$

$$z=1: \qquad v'_z+w'_y+(Ma/Pr)(\theta'_y+\mathrm{D}\bar{\theta}\eta_y-c'_y-\mathrm{D}\bar{c}\eta_y)=0, \tag{2.14e}$$

$$z=1: \qquad 2w'_z-p'-\mathrm{D}\bar{p}\eta-\Sigma[1-Ca(\bar{\theta}-\bar{c})](\eta_{xx}+\eta_{yy})=0, \tag{2.14f}$$

$$z=1: \qquad \theta'_z+Bi\theta'+Bi\mathrm{D}\bar{\theta}\eta=0, \tag{2.14g}$$

$$z=1: \qquad c'_z-\chi Bi\theta'-\chi Bi\mathrm{D}\bar{\theta}\eta=0. \tag{2.14h}$$

Here, $\mathrm{D}=\mathrm{d}/\mathrm{d}z$. For most common liquids, the capillary number has very small values ($Ca\ll 1$).

We expand the three-dimensional infinitesimal perturbations in the form of normal modes

$$(u',v',w',p',\theta',c',\eta)=[\hat{u}(z),\hat{v}(z),\hat{w}(z),\hat{p}(z),\hat{\theta}(z),\hat{c}(z),\hat{\eta}]\mathrm{e}^{\mathrm{i}(k_x x+k_y y-\omega t)}, \tag{2.15}$$

where k_x and k_y are the complex wavenumbers in the x- and y-directions, and ω is the complex frequency. Substituting these expressions into the linearized perturbation equations (2.13) and linearized boundary conditions (2.14), we obtain the linear stability equations expressed in primitive variables,

$$\mathrm{i}k_x\hat{u}+\mathrm{i}k_y\hat{v}+\mathrm{D}\hat{w}=0, \tag{2.16a}$$

$$-\mathrm{i}\omega\hat{u}+\mathrm{i}k_x\bar{u}\hat{u}+\mathrm{D}\bar{u}\hat{w}=-\mathrm{i}k_x\hat{p}+(\mathrm{D}^2-k^2)\hat{u}, \tag{2.16b}$$

$$-\mathrm{i}\omega\hat{v}+\mathrm{i}k_x\bar{u}\hat{v}=-\mathrm{i}k_y\hat{p}+(\mathrm{D}^2-k^2)\hat{v}, \tag{2.16c}$$

$$-\mathrm{i}\omega\hat{w}+\mathrm{i}k_x\bar{u}\hat{w}=-\mathrm{D}\hat{p}+(\mathrm{D}^2-k^2)\hat{w}, \tag{2.16d}$$

$$Pr(-\mathrm{i}\omega\hat{\theta}+\mathrm{i}k_x\bar{u}\hat{\theta}+\mathrm{D}\bar{\theta}\hat{w})=(\mathrm{D}^2-k^2)\hat{\theta}, \tag{2.16e}$$

$$Sc(-\mathrm{i}\omega\hat{c}+\mathrm{i}k_x\bar{u}\hat{c}+\mathrm{D}\bar{c}\hat{w})=(\mathrm{D}^2-k^2)\hat{c}+\chi(\mathrm{D}^2-k^2)\hat{\theta}, \tag{2.16f}$$

and the boundary conditions

$$\hat{u}(0)=\hat{v}(0)=\hat{w}(0)=\hat{\theta}(0)=0, \tag{2.17a}$$

$$\mathrm{D}\hat{c}(0)+\chi\mathrm{D}\hat{\theta}(0)=0, \tag{2.17b}$$

$$-\mathrm{i}\omega\hat{\eta}+\mathrm{i}k_x\bar{u}(1)\hat{\eta}-\hat{w}(1)=0, \tag{2.17c}$$

$$\mathrm{D}\hat{u}(1)+\mathrm{i}k_x\hat{w}(1)+\mathrm{D}^2\bar{u}(1)\hat{\eta}+\mathrm{i}k_x\frac{Ma}{Pr}[\hat{\theta}(1)+\mathrm{D}\bar{\theta}(1)\hat{\eta}-\hat{c}(1)-\mathrm{D}\bar{c}(1)\hat{\eta}]=0, \tag{2.17d}$$

$$\mathrm{D}\hat{v}(1)+\mathrm{i}k_y\hat{w}(1)+\mathrm{i}k_y\frac{Ma}{Pr}[\hat{\theta}(1)+\mathrm{D}\bar{\theta}(1)\hat{\eta}-\hat{c}(1)-\mathrm{D}\bar{c}(1)\hat{\eta}]=0, \tag{2.17e}$$

$$2\mathrm{D}\hat{w}(1)-\hat{p}(1)-\mathrm{D}\bar{p}(1)\hat{\eta}+\Sigma[1-Ca(\theta(\bar{1})-\bar{c}(1))]k^2\hat{\eta}=0, \tag{2.17f}$$

$$\mathrm{D}\hat{\theta}(1)+Bi\hat{\theta}(1)+Bi\mathrm{D}\bar{\theta}(1)\hat{\eta}=0, \tag{2.17g}$$

$$\mathrm{D}\hat{c}(1)-\chi Bi\hat{\theta}(1)-\chi Bi\mathrm{D}\bar{\theta}(1)\hat{\eta}=0, \tag{2.17h}$$

where $k^2 = k_x^2 + k_y^2$. From (2.16*a*)–(2.16*d*), it can be easily shown that

$$2\mathrm{i}k_x \mathrm{D}\bar{u}\hat{w} = -(\mathrm{D}^2 - k^2)\hat{p}. \tag{2.18}$$

Combining (2.16*d*) and (2.18), we can obtain the generalized Orr–Sommerfeld equation

$$(\mathrm{D}^2 - k^2)^2\hat{w} = \mathrm{i}[(\bar{u}k_x - \omega)(\mathrm{D}^2 - k^2) - \mathrm{D}^2\bar{u}k_x]\hat{w}. \tag{2.19}$$

Finally, the full system of linear stability equations with respect to the eigenfunctions $\hat{w}$, $\hat{\theta}$ and $\hat{c}$ is given by

$$(\mathrm{D}^2 - k^2)^2\hat{w} = \mathrm{i}[(\bar{u}k_x - \omega)(\mathrm{D}^2 - k^2) - \mathrm{D}^2\bar{u}k_x]\hat{w}, \tag{2.20a}$$

$$Pr[\mathrm{i}(\bar{u}k_x - \omega)\hat{\theta} + \mathrm{D}\bar{\theta}\hat{w}] = (\mathrm{D}^2 - k^2)\hat{\theta}, \tag{2.20b}$$

$$Sc\,[\mathrm{i}(\bar{u}k_x - \omega)\hat{c} + \mathrm{D}\bar{c}\hat{w}] = (\mathrm{D}^2 - k^2)\hat{c} + \chi(\mathrm{D}^2 - k^2)\hat{\theta}, \tag{2.20c}$$

$$\hat{w}(0) = \mathrm{D}\hat{w}(0) = \hat{\theta}(0) = 0, \tag{2.20d}$$

$$\mathrm{D}\hat{c}(0) + \chi\mathrm{D}\hat{\theta}(0) = 0, \tag{2.20e}$$

$$\mathrm{i}[\bar{u}(1)k_x - \omega]\hat{\eta} - \hat{w}(1) = 0, \tag{2.20f}$$

$$(\mathrm{D}^2 + k^2)\hat{w}(1) - \mathrm{i}k_x\mathrm{D}^2\bar{u}(1)\hat{\eta} + k^2\frac{Ma}{Pr}[\hat{\theta}(1) + \mathrm{D}\bar{\theta}(1)\hat{\eta} - \hat{c}(1) - \mathrm{D}\bar{c}(1)\hat{\eta}] = 0, \tag{2.20g}$$

$$[\mathrm{D}^2 - 3k^2 - \mathrm{i}(\bar{u}(1)k_x - \omega)]\mathrm{D}\hat{w}(1) + [\mathrm{D}\bar{p}(1) - \Sigma' k^2]k^2\hat{\eta} = 0, \tag{2.20h}$$

$$\mathrm{D}\hat{\theta}(1) + Bi\hat{\theta}(1) + Bi\mathrm{D}\bar{\theta}(1)\hat{\eta} = 0, \tag{2.20i}$$

$$\mathrm{D}\hat{c}(1) - \chi Bi\hat{\theta}(1) - \chi Bi\mathrm{D}\bar{\theta}(1)\hat{\eta} = 0, \tag{2.20j}$$

with $\Sigma' = \Sigma[1 - Ca(\bar{\theta}(1) - \bar{c}(1))]$.

The linear stability equations (2.20) are ordinary differential equations in terms of $\hat{w}$, $\hat{\theta}$, $\hat{c}$ and $\hat{\eta}$, and can be regarded as a two-point boundary value problem. If there exists a non-trivial solution for the equations, a corresponding dispersion relation

$$\mathrm{D}(k_x, k_y, \omega; Ka, G, Pr, L, \chi, M, B, \beta) = 0$$

should be satisfied, and we need to solve an eigenvalue problem. Because it is impossible to find the explicit analytical dispersion relation if there is no further simplification, the dispersion relation has to be obtained numerically. In this paper, the pseudospectral Chebyshev method (Canuto *et al.* 1988) is used to discretize the eigenvalue problem, and the QZ algorithm is used to solve the resulting general eigenvalue problem. A mapping technique (Pearlstein & Goussis 1988) is used to map the infinite spurious eigenvalues due to the boundary conditions (2.20*d*) and (2.20*e*) to a specified point in the complex plane.

Note that the following temporal and spatio-temporal stability analyses of the film flow have been performed for a fixed inclination of the plate ($\beta = 15^\circ$) and fixed values of the Kapitza, Prandtl, Lewis and Biot numbers ($Ka = 500$, $Pr = 10$, $L = 0.01$, $B = 0.02$).

3. Temporal instability

When the Soret number is equal to zero, i.e. $\chi = 0$, the problem is reduced to the situation where the solutal Marangoni effect (induced by the variations of solute concentration along the free surface) is not taken into account. In this case, when the incline angle is sufficiently large and in the long-wavelength limit, it was shown that

the flow becomes first unstable with respect to transverse waves which extract the maximum amount of energy from the basic state (Kelly, Davis & Goussis 1986; Kelly *et al.* 1989), while, for small angles of inclination, the unstable disturbance assumes the form of longitudinal rolls (Sreenivasan & Lin 1978). Later, Goussis & Kelly (1991) pointed out that the instability can assume the form of either long transverse waves or short longitudinal rolls depending on which mechanism (connected to H-, S- or P-modes) is dominant. In our case, we select a moderate incline angle, $\beta = 15^\circ$, and study the influence of the solutal Marangoni effect on the destabilization of the flow by both pure streamwise perturbations (transverse rolls) and pure spanwise perturbations (longitudinal rolls).

Results concerning the destabilization of the flow by fully three-dimensional perturbations could be theoretically obtained from a pure streamwise study. As already indicated by Goussis & Kelly (1991) for $\chi = 0$, the Squire theorem is not valid, but a Squire transformation exists, which is also valid with solutal effects. This Squire transformation corresponds to the relations $k^2 = k_x^2 + k_y^2$, $k\,G\,\sin(\beta) = k_x\,G_{3d}\,\sin(\beta_{3d})$ and $G\,\cos(\beta) = G_{3d}\,\cos(\beta_{3d})$. It gives a clear connection between the results for three-dimensional instabilities (or oblique wave instabilities) with a wave vector of arbitrary orientation (arbitrary values of k_x and k_y) and those for the streamwise instabilities (with a wave vector k along x). In these relations, G and β are the parameters corresponding to the streamwise instabilities, whereas G_{3d} and β_{3d} are the parameters corresponding to the three-dimensional instabilities. These relations also indicate that the results for three-dimensional instabilities correspond to results obtained for streamwise perturbations at smaller Galileo numbers and smaller incline angles. Although all the results can be derived from the study of the streamwise perturbations, it would be necessary to widely vary both the inclination β and the Galileo number G. Our choice to fix β does not allow derivation of the results for any three-dimensional perturbations and leads us to focus on the usual streamwise and spanwise perturbations.

3.1. *Pure streamwise perturbations: $k_y = 0$ and $k = k_x$*

The system (2.20) with $k = k_x$ becomes

$$(\mathrm{D}^2 - k^2)^2\hat{w} = \mathrm{i}[(\bar{u}k - \omega)(\mathrm{D}^2 - k^2) - \mathrm{D}^2\bar{u}k]\hat{w}, \tag{3.1a}$$

$$Pr[\mathrm{i}(\bar{u}k - \omega)\hat{\theta} + \mathrm{D}\bar{\theta}\hat{w}] = (\mathrm{D}^2 - k^2)\hat{\theta}, \tag{3.1b}$$

$$Sc[\mathrm{i}(\bar{u}k - \omega)\hat{c} + \mathrm{D}\bar{c}\hat{w}] = (\mathrm{D}^2 - k^2)\hat{c} + \chi(\mathrm{D}^2 - k^2)\hat{\theta}, \tag{3.1c}$$

$$\hat{w}(0) = \mathrm{D}\hat{w}(0) = \hat{\theta}(0) = 0, \tag{3.1d}$$

$$\mathrm{D}\hat{c}(0) + \chi\,\mathrm{D}\hat{\theta}(0) = 0, \tag{3.1e}$$

$$\mathrm{i}[\bar{u}(1)k - \omega]\hat{\eta} - \hat{w}(1) = 0, \tag{3.1f}$$

$$(\mathrm{D}^2 + k^2)\hat{w}(1) - \mathrm{i}k\mathrm{D}^2\bar{u}(1)\hat{\eta} + k^2\frac{Ma}{Pr}[\hat{\theta}(1) + \mathrm{D}\bar{\theta}(1)\hat{\eta} - \hat{c}(1) - \mathrm{D}\bar{c}(1)\hat{\eta}] = 0, \tag{3.1g}$$

$$[\mathrm{D}^2 - 3k^2 - i(\bar{u}(1)k - \omega)]\mathrm{D}\hat{w}(1) + [\mathrm{D}\bar{p}(1) - \Sigma' k^2]k^2\hat{\eta} = 0, \tag{3.1h}$$

$$\mathrm{D}\hat{\theta}(1) + Bi\hat{\theta}(1) + Bi\mathrm{D}\bar{\theta}(1)\hat{\eta} = 0, \tag{3.1i}$$

$$\mathrm{D}\hat{c}(1) - \chi Bi\hat{\theta}(1) - \chi Bi\mathrm{D}\bar{\theta}(1)\hat{\eta} = 0. \tag{3.1j}$$

As it is not possible to find an analytical neutral relation from the linear stability equations (3.1), we use the Chebyshev spectral collocation method to compute the numerical dispersion relations associated with (3.1) and then obtain the neutral curves

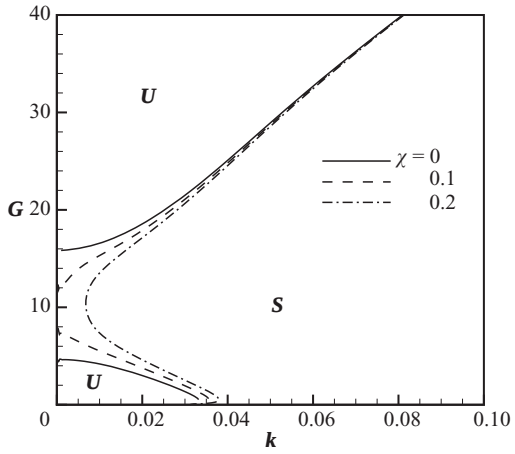

FIGURE 2. Neutral curves for the streamwise instabilities in the G–k parameter space for different Soret numbers χ and $M = 50$. The upper unstable domain of the H-mode instability and the lower unstable domain of the S-mode instability merge when χ is increased ($Ka = 500$, $Pr = 10$, $L = 0.01$, $B = 0.02$, $\beta = 15^\circ$). U denotes an unstable domain and S a stable one.

from them. The neutral curves of temporal instability for streamwise perturbations are plotted in the G–k parameter space in figures 2 and 4 for $M = 50$ and $M = 100$, respectively, and for different Soret numbers ($Ka = 500$, $Pr = 10$, $L = 0.01$, $B = 0.02$, $\beta = 15^\circ$). We first see that larger Soret numbers make the flow system more unstable, particularly for moderate Galileo numbers. For the situation at $M = 50$ (figure 2) where only long-wave unstable regions are found, the results show that for $\chi = 0$, two separate unstable regions appear, one below a critical Galileo number which corresponds to the S-mode of thermocapillary instability, and the other above another critical Galileo number which corresponds to the H-mode of surface wave instability. On increasing the Soret number the two critical Galileo numbers approach one another, until the merging of the two neutral curves and the connection between the two unstable regions of S- and H-modes. Such a behaviour was observed by Goussis & Kelly (1991) for $\chi = 0$ and was obtained by increasing the Marangoni number M. As usual, the long-wave approximation of Yih (1963) can be used to obtain the critical Galileo numbers at zero wavenumber. The corresponding neutral relation at $k = 0$ is given by

$$(G \sin\beta)^2 - \frac{5}{2} G \cos\beta + \frac{15}{64} \frac{(3\chi Bi + 12\chi + 16) MaBi}{Pr(1 + Bi)^2} = 0 \tag{3.2}$$

or

$$(G \sin\beta)^2 - \frac{5}{2} G \cos\beta + \frac{15}{64} \frac{(3\chi BG^{1/3} + 12\chi + 16) MBG^{2/3}}{(1 + BG^{1/3})^2} = 0, \tag{3.3}$$

the detailed derivation being given in Appendix B. Note that the relation (3.3) is independent of the Kapitza, Prandtl, and Lewis numbers. From figure 3, where, in the long-wave limit (3.3), the critical Galileo number G_c is plotted as a function of χ for different Marangoni numbers M, we see that above a cutoff positive Soret number the film flow is always long-wave unstable for any Galileo number G. The cutoff Soret number decreases with the increase of the Marangoni number, and it is already negative for $M = 60$, indicating that the long-wave instability exists at $\chi = 0$ for all Galileo numbers in this case. The same observation can be made for larger Marangoni

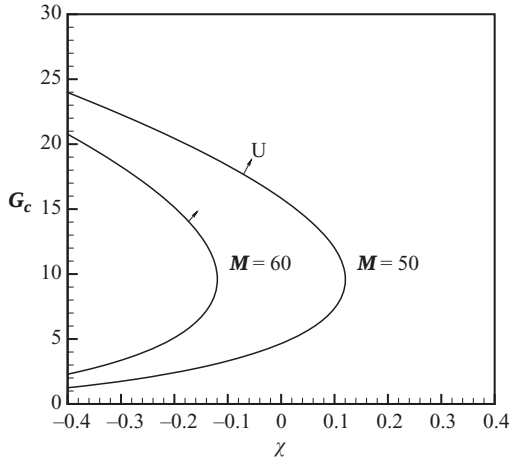

FIGURE 3. Critical Galileo number G_c as a function of the Soret number χ for the streamwise instabilities in the long-wave limit (3.3) for different Marangoni numbers. The arrows indicate the unstable side of the curves. It is shown that above a certain value of χ the situation is long-wave unstable for any Galileo number ($Ka = 500$, $Pr = 10$, $L = 0.01$, $B = 0.02$, $\beta = 15°$); relation (3.3) is independent of Ka, Pr, and L.

numbers as shown by the neutral curves obtained for $M = 100$ (figure 4*a*). Note that for this value of M, the neutral curve for the P-mode of thermocapillary instability can be detected, and appears to be very sensitive to the influence of the Soret effect with a strong decrease of the critical Galileo number (minimum value of G on the neutral curve) (figure 4*b*). To characterize the general influence of χ on the different modes, we can say that the positive values of χ chosen increase the Marangoni effect in conjunction with the Marangoni number M. This influence is explicitly shown in the relation (3.3) for the long-wave limit case. Concerning particularly the P-mode, the evolution with χ does not significantly change the critical wavenumber k associated with the critical G. This is consistent with the study of Hu, Ben Hadid & Henry (2007) concerning the Poiseuille–Rayleigh–Bénard flow, where it is shown that the usual decrease of the critical wavenumber with the increase of the Soret number (which is also observed in the Marangoni–Bénard situation) is inhibited when the throughflow is applied.

Finally, by using the lubrication theory, a three-dimensional long-wave evolution equation for the dimensionless thickness of the film h can be derived as

$$h_t + Reh^2h_x + \varepsilon\left[\tfrac{2}{15}Re^2h^6h_x\right]_x - \varepsilon\nabla\cdot\left[\tfrac{1}{3}Re\cot\beta h^3\nabla h\right] + \varepsilon\tfrac{1}{3}\Gamma\nabla\cdot[h^3\nabla\nabla^2 h] + \varepsilon\frac{1}{2}\frac{Ma}{Pr}\nabla\cdot\left[\frac{(16+12\chi+3\chi Bih)Bih^2\nabla h}{16(1+Bih)^2}\right] + O(\varepsilon^2) = 0, \quad (3.4)$$

where $\nabla = (\partial_x, \partial_y)$, $\Gamma = \varepsilon^2\Sigma'$ and ε is the ratio of the average thickness of the thin film d and the characteristic long wavelength λ. If we do the linear stability analysis from this long-wave evolution equation (3.4), the neutral relation (3.2) derived for $k \to 0$ can be recovered.

3.2. *Pure spanwise perturbations: $k_x = 0$ and $k = k_y$*

From the Squire transformation mentioned at the beginning of the section, we can show that the results for the inclined film subjected to spanwise perturbations ($k_x = 0$)

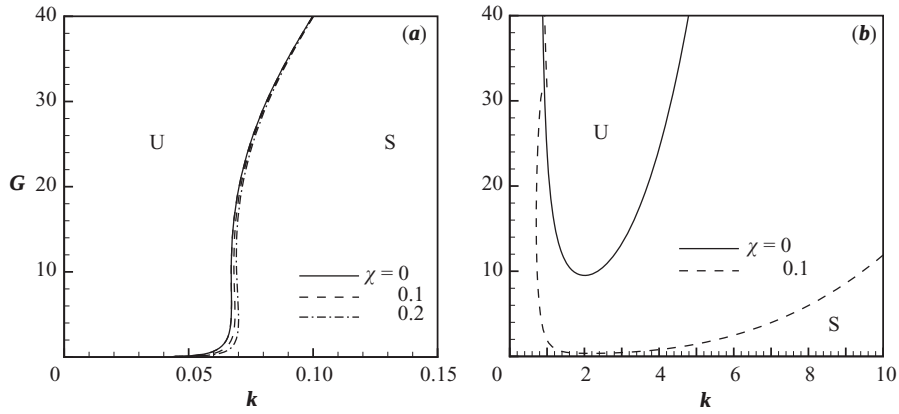

FIGURE 4. Neutral curves for the streamwise instabilities in the G–k parameter space for different Soret numbers χ and $M = 100$: (a) neutral curves for the merged H- and S-modes; (b) neutral curves for the P-mode ($Ka = 500$, $Pr = 10$, $L = 0.01$, $B = 0.02$, $\beta = 15°$).

correspond to the results obtained for streamwise perturbations at $\beta = 0$ and with $G = G_{3d}\cos(\beta_{3d})$ (3d referring here to the spanwise perturbations in the inclined film). The results for spanwise perturbations in the inclined film are thus identical to those obtained in a horizontal layer when the hydrostatic effect connected to G is taken into account in the model of the horizontal layer, and bearing in mind that the hydrostatic effect in the inclined film is connected to $G_{3d}\cos(\beta_{3d})$, i.e. is modified by the inclination of the film. In any case, for these situations, there is no mean flow, and the instability is of thermocapillary origin with no preferred direction of propagation. The system (2.20) with $k_x = 0$ becomes

$$(\mathrm{D}^2 - k^2)^2\hat{w} = -\mathrm{i}\omega(\mathrm{D}^2 - k^2)\hat{w}, \tag{3.5a}$$

$$(\mathrm{D}^2 - k^2)\hat{\theta} = Pr[-\mathrm{i}\omega\hat{\theta} + \mathrm{D}\bar{\theta}\hat{w}], \tag{3.5b}$$

$$(\mathrm{D}^2 - k^2)\hat{c} + \chi(\mathrm{D}^2 - k^2)\hat{\theta} = Sc[-\mathrm{i}\omega\hat{c} + \mathrm{D}\bar{c}\hat{w}], \tag{3.5c}$$

$$\hat{w}(0) = \mathrm{D}\hat{w}(0) = \hat{\theta}(0) = 0, \tag{3.5d}$$

$$\mathrm{D}\hat{c}(0) + \chi\mathrm{D}\hat{\theta}(0) = 0, \tag{3.5e}$$

$$\mathrm{i}\omega\hat{\eta} + \hat{w}(1) = 0, \tag{3.5f}$$

$$(\mathrm{D}^2 + k^2)\hat{w}(1) + k^2\frac{Ma}{Pr}[\hat{\theta}(1) + \mathrm{D}\bar{\theta}(1)\hat{\eta} - \hat{c}(1) - \mathrm{D}\bar{c}(1)\hat{\eta}] = 0, \tag{3.5g}$$

$$[\mathrm{D}^2 - 3k^2 + \mathrm{i}\omega]\mathrm{D}\hat{w}(1) + [\mathrm{D}\bar{p}(1) - \Sigma' k^2]k^2\hat{\eta} = 0, \tag{3.5h}$$

$$\mathrm{D}\hat{\theta}(1) + Bi\hat{\theta}(1) + Bi\mathrm{D}\bar{\theta}(1)\hat{\eta} = 0, \tag{3.5i}$$

$$\mathrm{D}\hat{c}(1) - \chi Bi\hat{\theta}(1) - \chi Bi\mathrm{D}\bar{\theta}(1)\hat{\eta} = 0. \tag{3.5j}$$

Moreover, if we assume that the marginal state is stationary, i.e. $\omega = 0$, the system (3.5) yields an analytical solution. From the stability equations (3.5a), (3.5b) and (3.5c), we

can obtain the general form of the solutions:

$$\hat{w} = 2[A_2 + kB_1 + 2kB_2 z]\cosh(kz) + 2[B_2 + kA_1 + 2kA_2 z]\sinh(kz), \tag{3.6a}$$

$$\hat{\theta} = -\frac{PrBi}{1+Bi}\left\{[A_0 + A_1 z + A_2 z^2]\cosh(kz) + [B_0 + B_1 z + B_2 z^2]\sinh(kz)\right\} \tag{3.6b}$$

$$\begin{aligned}\hat{c} = \frac{ScBi\chi}{1+Bi}\big\{&[(LA_0 + A_0') + (L+1)A_1 z + (L+1)A_2 z^2]\cosh(kz) \\ &+ [(LB_0 + B_0') + (L+1)B_1 z + (L+1)B_2 z^2]\sinh(kz)\big\}.\end{aligned} \tag{3.6c}$$

The neutral curve is then formulated as

$$Sc\left(\frac{F_1}{M^*} - F_2\right)\left(G\cos\beta + \Sigma' k^2\right) = F_3, \tag{3.7}$$

where

$$\begin{aligned} M^* &= \frac{BiMa}{1+Bi}, \\ F_1 &= 8Lk^2(\sinh k\cosh k - k)(Bi\sinh k + k\cosh k)\sinh k, \\ F_2 &= [Bi\chi\cosh k + (L + \chi + L\chi)k\sinh k](\sinh^3 k - k^3\cosh k) \\ &\quad + \chi k\left[Bi(k^2 + k\sinh k\cosh k - 2\sinh^2 k) + (k\cosh k - \sinh k)^2\right], \\ F_3 &= 8(\chi+1)k^6\sinh k\cosh k. \end{aligned}$$

In the limit $k \to 0$, (3.7) can be reduced to

$$\left[\frac{16L(Bi+1)}{3M^*} - \left(\frac{Bi}{24} + \frac{1}{9}\right)\chi\right] Sc\, G\cos\beta = 8(\chi+1) \tag{3.8}$$

or

$$\left[\frac{16(B\,G^{1/3}+1)^2}{3MB\,G^{2/3}} - \left(\frac{B\,G^{1/3}}{24} + \frac{1}{9}\right) Sc\,\chi\right] G\cos\beta = 8(\chi+1). \tag{3.9}$$

If we impose $Bi = 0$, (3.8) reduces to equation (28) given by Joo (1995). Furthermore, when $\chi = 0$, i.e. without considering the Soret effect, (3.7) and (3.8) reduce to equations (16) and (17) of Goussis & Kelly (1991). And similarly to the case $\chi = 0$, (3.8) shows that $G \to \infty$ when $\beta \to 90^\circ$, indicating that the layer is unstable for all G in this limit.

Using the formulation (3.7), we first plot the neutral curves of temporal instability in the G–k parameter space for different small Soret numbers χ and for $M = 50$ ($Ka = 500$, $Pr = 10$, $L = 0.01$, $B = 0.02$, $\beta = 15^\circ$) (figure 5). As already known from the previous studies for $\chi = 0$ (Goussis & Kelly 1991), the long-wave unstable region in figure 5(a) corresponds to the S-mode of thermocapillary instability, while the unstable region in figure 5(b) corresponds to the P-mode of thermocapillary instability. It is, first, interesting to note that on increasing the Soret number χ, the unstable regions for both modes become larger. Then, for the P-mode, the evolution of the neutral curve for positive Soret numbers leads to the appearance of a long-wave instability above a critical Galileo number G_c which decreases as χ is increased. Finally, for a large enough Soret number, the S-mode and P-mode neutral curves will merge at zero wavenumber, and above this cutoff positive Soret number, the film flow will always be long-wave unstable for any Galileo number G. This can be easily verified from figure 6 where, in the long-wave limit (3.9), the critical Galileo number G_c for the stationary spanwise instabilities is plotted as a function of χ for different Marangoni numbers (solid lines). The cutoff Soret number is also found to decrease with the

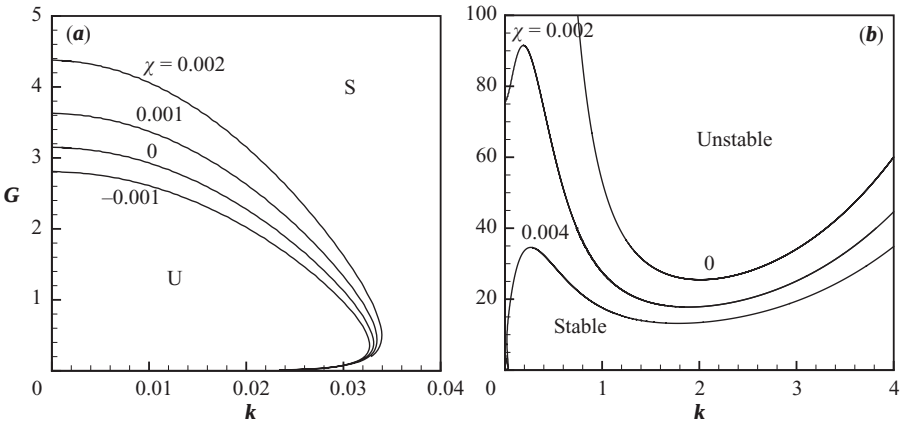

FIGURE 5. Neutral curves for the stationary spanwise instabilities in the G–k parameter space for different Soret numbers χ and $M = 50$: (a) neutral curves for the long-wave S-mode; (b) neutral curves for the P-mode, which merge with the curves of the S-mode for $\chi = 0.004$ ($Ka = 500$, $Pr = 10$, $L = 0.01$, $B = 0.02$, $\beta = 15°$).

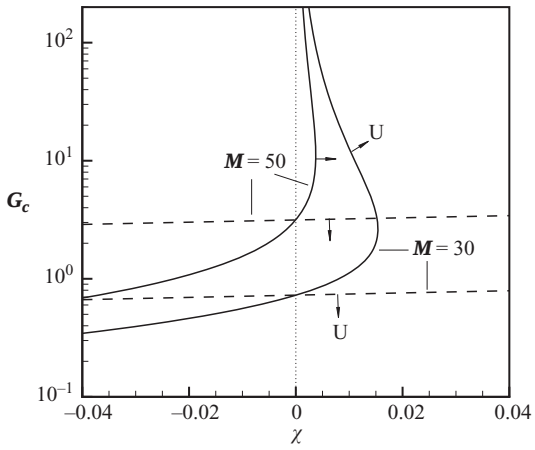

FIGURE 6. Critical Galileo number G_c as a function of the Soret number χ for the spanwise stationary (solid lines) and oscillatory (dashed lines) instabilities in the long-wave limit for different Marangoni numbers. The arrows indicate the unstable side of the curves. The dotted line represents $\chi = 0$. It is shown that above a certain value of χ the situation is long-wave unstable with respect to the stationary instabilities for any Galileo number, and that the oscillatory modes are more unstable than the stationary modes for negative values of χ ($Ka = 500$, $Pr = 10$, $L = 0.01$, $B = 0.02$, $\beta = 15°$).

increase of the Marangoni number: its value which is about 0.0154 for $M = 30$ decreases to 0.00373 for $M = 50$. This effect seems similar to what was observed for streamwise perturbations with the connection between the two unstable regions of S- and H-modes. Nevertheless, we can note that for those long-wave instabilities, the results for spanwise perturbations are much more sensitive to the influence of the Soret effect than those for streamwise perturbations (the values of χ necessary to clearly affect the results are about 0.1 in the second case, and less than 0.01 in the first case). Moreover, the decrease of the wavenumber of the P-mode from finite values towards zero when χ is increased from zero is similar to what has already been

ω_r	ω_i
0.0000000000	0.0000000000
0.0000000000	−0.0123966400
0.0000000000	−0.0459176405
0.0000000000	−0.0956284934
0.0000000000	−0.1255543009
0.0000000000	−0.1602111422
0.0000000000	−0.2505393668
0.0000000000	−0.3592242951
0.0000000000	−0.4876022552
0.0000000000	−0.6356464550

TABLE 1. Most unstable eigenvalues for a state belonging to the neutral curve for the stationary spanwise instability: $k = 2$, $G = 17.861614664$, $\chi = 0.002$, and $M = 50$ ($Ka = 500$, $Pr = 10$, $L = 0.01$, $B = 0.02$, $\beta = 15^\circ$).

observed in Marangoni–Bénard and Rayleigh–Bénard situations for small values of the Lewis number.

In order to prove that the neutral curve for $\omega = 0$ really corresponds to the most dangerous mode, one possibility is to compute the first eigenvalues with the largest imaginary parts for states belonging to the neutral curve and to verify that $\omega = 0$ is the most unstable eigenvalue. An example of this verification is shown in table 1 for the set of parameters, $k = 2.0$, $G = 17.861614664$, $\chi = 0.002$, $M = 50$, $Ka = 500$, $Pr = 10$, $L = 0.01$, $B = 0.02$, and $\beta = 15^\circ$ which satisfy relation (3.7) of the neutral curve. In this way, we have proved that, for $\chi \geqslant 0$, the neutral curves obtained for $\omega = 0$ correspond to the most dangerous mode, or, in other words, that, for $\chi \geqslant 0$, the real neutral curves for the spanwise perturbations correspond to stationary modes.

In the horizontal situation (but without the hydrostatic effect), Joo (1995) showed that for combined destabilizing thermal Marangoni effect and stabilizing solutal Marangoni effect, long-wave oscillatory instabilities can be obtained which are preferred to the long-wave stationary instabilities. In a similar situation, but with a fixed heat flux across the layer, it has also been revealed by Podolny *et al.* (2005, 2006) that there is a negative value of the Soret number below which a long-wave oscillatory instability is obtained for positive Marangoni numbers. In our case of spanwise instabilities in an inclined film, which is similar to the horizontal case (see our remarks above), a long-wave oscillatory mode is also found for negative Soret numbers. The corresponding neutral curves in the G–k parameter space are plotted in figure 7 for $M = 50$ and different Soret numbers χ. We see that there exists a critical Galileo number in the long-wave limit, below which the flow is unstable with respect to the long-wave oscillatory instability, and this critical Galileo number decreases as the absolute value of the Soret number increases. The value of the critical Galileo number can be obtained from a relation easily derived from (3.3). As already indicated, the case of spanwise perturbations can be obtained from the case of streamwise perturbations by putting $k_x = 0$ in the Squire relations, which gives $\beta = 0$ and $G = G_{3d} \cos(\beta_{3d})$ ($3d$ referring here to the spanwise perturbations). This leads to a relation similar to (3.3) but without the first term $G \sin\beta$, valid for the spanwise perturbations in the long-wave limit.

For the set of parameters, $k = 0.02$, $\chi = -0.04$, $G = 2.058$, $M = 50$, $Ka = 500$, $Pr = 10$, $L = 0.01$, $B = 0.02$ and $\beta = 15^\circ$, corresponding to a state on the neutral curve obtained for $\chi = -0.04$, the first eigenvalues with largest imaginary parts have been computed

ω_r	ω_i
−0.00001259	0.00000000
0.00001259	0.00000000
0.00000000	−0.00986486
0.00000000	−0.03947761
0.00000000	−0.08882613
0.00000000	−0.15791398
0.00000000	−0.24673555
0.00000000	−0.25204745
0.00000000	−0.35530571
0.00000000	−0.48361103

TABLE 2. Most unstable eigenvalues for a state belonging to the neutral curve for the oscillatory long-wave spanwise instability: $k = 0.02$, $G = 2.058$, $\chi = -0.04$, and $M = 50$ ($Ka = 500$, $Pr = 10$, $L = 0.01$, $B = 0.02$, $\beta = 15°$).

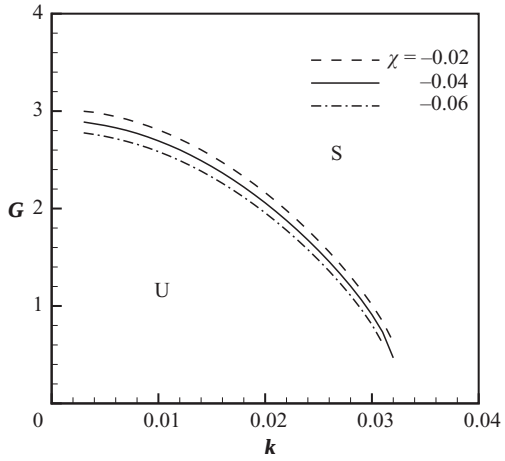

FIGURE 7. Neutral curves for the oscillatory spanwise long-wave instabilities in the G–k parameter space for different Soret numbers χ and $M = 50$ ($Ka = 500$, $Pr = 10$, $L = 0.01$, $B = 0.02$, $\beta = 15°$).

and are presented in table 2. We verify that for this state at $\chi = -0.04$ the oscillatory instability is the most dangerous mode. In fact, as shown in figure 6 where, in the long-wave limit, the critical Galileo numbers for both stationary and oscillatory instabilities are plotted as a function of χ, the oscillatory mode is more unstable than the stationary mode for negative χ; when $\chi = 0$, the critical Galileo numbers for both instabilities are identical as the relation (3.3) (without the first term) for the oscillatory instability is exactly the same as the relation (3.9) for the stationary instability. This result is in good agreement with the results of Goussis & Kelly (1991) obtained without the Soret effect.

Apart from this oscillatory long-wave instability, there also exists an oscillatory short-wave instability for negative Soret numbers. This instability was not mentioned by Joo (1995), but appears in the usual evolution of the stationary short-wave P-mode instability (see figure 5) for stabilizing solutal effect (negative χ), as it occurs in the classical Marangoni–Bénard and Rayleigh–Bénard situations. The neutral curves for this short-wave oscillatory mode are plotted in the G–k parameter space in figure 8 for

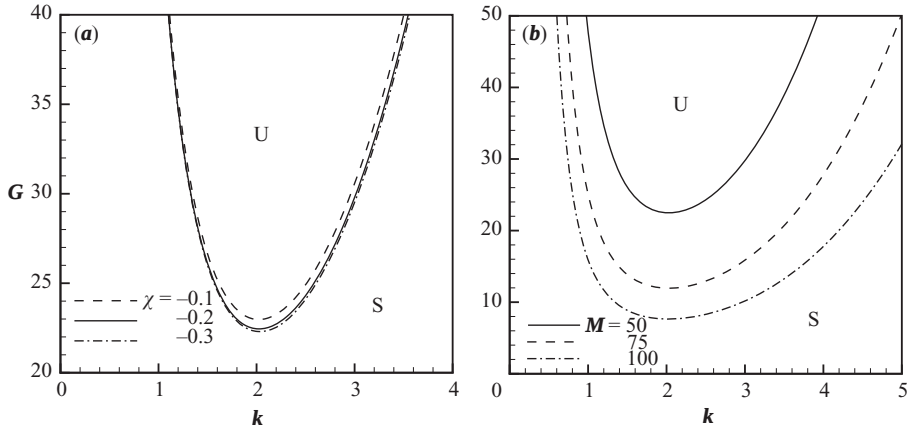

FIGURE 8. Neutral curves for the oscillatory spanwise short-wave instabilities in the G–k parameter space: (a) neutral curves for different Soret numbers χ and $M = 50$; (b) neutral curves for different Marangoni numbers M and $\chi = -0.2$ ($Ka = 500$, $Pr = 10$, $L = 0.01$, $B = 0.02$, $\beta = 15°$).

different Soret numbers at $M = 50$ and different Marangoni numbers at $\chi = -0.2$. We see that the critical Galileo number decreases slowly with the increase of the absolute value of the Soret number, while it decreases much faster with the increase of the Marangoni number. The corresponding critical wavenumber does not vary much and remains around 2, close to the value for the stationary P-mode instability at $\chi = 0$, similarly to what is found in the classical Marangoni–Bénard and Rayleigh–Bénard situations. Owing to the invariance of the basic flow in the spanwise direction, both long-wave and short-wave oscillatory instabilities are associated with two unstable modes with opposite frequencies, i.e. corresponding to right- and left-travelling waves.

4. Absolute and convective instability

Before we consider the spatio-temporal instability of the binary liquid film flow, let us recall the basic concepts of the absolute/convective instability theory (AI/CI) which originated from plasma physics (Briggs 1964; Bers 1973). A good introduction to this theory can be found in Huerre & Monkewitz (1985, 1990) who first applied such a spatio-temporal stability analysis to spatially developing flows. They analytically investigated the absolute/convective nature of the instability through the asymptotic response of the Green function at large time. Furthermore, they indicated that periodic forcing on the boundary can be spatially amplified only when the system is convectively unstable.

Basically, when an amplifying wave packet is convected away from its local position, the wave packet is said to be convectively unstable. If, otherwise, the amplification can be observed locally, the wave packet is said to be absolutely unstable. Generally, the absolute/convective nature of the instability is determined by the sign of the absolute growth rate $\omega_{0i} = \mathrm{Im}[\omega(k_0)]$ defined at the saddle point k_0 of the dispersion relation, i.e. when $(\mathrm{d}\omega/\mathrm{d}k)|_{k_0} = 0$. In these expressions, k is a complex wavenumber and ω is a complex frequency. If the absolute growth rate ω_{0i} is greater than zero (lower than zero), the flow is said to be absolutely (convectively) unstable. But it should be noted that the saddle point k_0 used to identify AI/CI must satisfy the

Briggs–Bers collision criterion, i.e. the saddle point must be a pinch point produced by two distinct spatial branches of solutions of the dispersion relation, $k_n^{\pm}(\omega)$, coming, respectively, from the upper and lower half-k-planes, and commonly referred to as upstream and downstream branches. In this paper the saddle points have all been found to satisfy the collision criterion. The processes of identification of the pinch points are not shown here, but they are presented in detail in Brevdo *et al.* (1999) for isothermal falling films.

From the above definitions, the boundary between absolute and convective instability is determined by a zero absolute growth rate, i.e. $\omega_{0i} = 0$. But, when we select a set of parameters, the absolute growth rate may be far from zero or may even not exist at all. In order to determine the parameters whose absolute growth rate is near zero, it is necessary to study the response of the flow to a localized disturbance along an arbitrary fixed spatio-temporal ray, $V = x/t$, as $t \to \infty$. This is equivalent to analysing how the response evolves in a reference frame moving at velocity V. If we introduce the Doppler-shifted frequency $\omega^v = \omega - Vk$ and use $k^v = k$, the dispersion relation in the moving coordinate system will be

$$\mathrm{D}_v(k^v, \omega^v) = \mathrm{D}(k^v, \omega^v + Vk^v) = 0. \tag{4.1}$$

As $\mathrm{d}\omega^v/\mathrm{d}k^v = 0$, the saddle point $\tilde{k}$ will occur at

$$\mathrm{D}(\tilde{k}, \tilde{\omega}) = 0 \quad \text{and} \quad \frac{\mathrm{d}\omega}{\mathrm{d}k}(\tilde{k}, \tilde{\omega}) = V, \tag{4.2}$$

and the local (absolute) growth rate in the moving frame is thus obtained at $k_0^v = \tilde{k}$ through

$$\omega_0^v = \tilde{\omega} - V\tilde{k}. \tag{4.3}$$

Here also, the saddle point $\tilde{k}$ obtained from (4.2) must verify the Briggs–Bers collision criterion mentioned above. The saddle points in this paper are obtained numerically by Newton-type iterations (Deissler 1987; Yin *et al.* 2000).

Of course the absolute growth rate in the laboratory frame is just the local growth rate for $V = 0$. Thus, through studying the effect of the dimensionless parameters on the local growth rates in the moving frame, we can obtain a set of parameters whose absolute growth rate is near zero. The boundary curve between absolute and convective instability can then be determined by a continuation procedure.

Note that we will focus our spatio-temporal study on the streamwise instabilities. The spanwise instabilities (which are not affected by the basic flow velocity), as suggested by the AI/CI boundary curves of the Poiseuille–Rayleigh–Bénard flow in binary fluids (Hu *et al.* 2007), should determine a direct absolute transition when they are stationary whereas they should first trigger a convective behaviour above the critical values of the parameters (such as Marangoni and Soret numbers) when they are oscillatory.

4.1. *Long-wave spatio-temporal instability of S- and H-modes*

We first consider the long-wave instability triggered by streamwise perturbations associated with S- and H-modes. In this case, the growth rate ω_{0i}^v will be calculated as a function of the ray velocity V in the streamwise direction x for different sets of parameters. As already indicated at the end of § 2, the parameters Ka, Pr, L, B, and β will be supposed fixed ($Ka = 500$, $Pr = 10$, $L = 0.01$, $B = 0.02$, and $\beta = 15^\circ$), and the other parameters G, M, and χ will be allowed to vary. The evolution of ω_{0i}^v with V is first shown for $\chi = 0$ (without the Soret effect) and $M = 100$ and

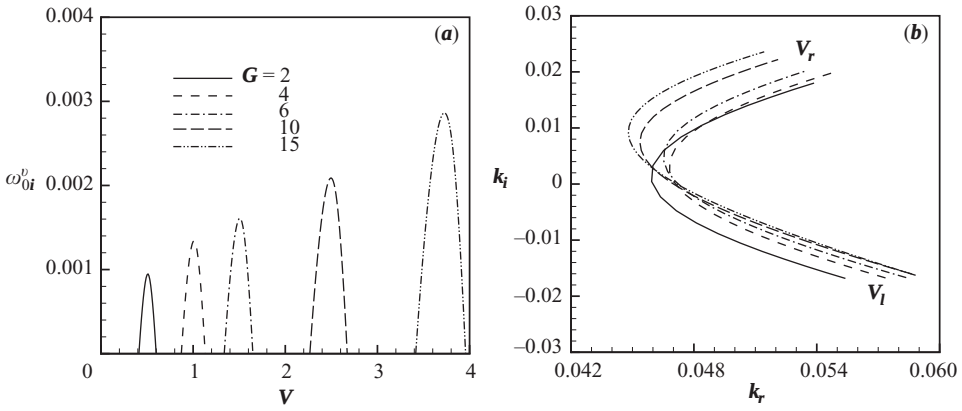

FIGURE 9. (*a*) Growth rate ω_{0i}^{v} as a function of the ray velocity V and (*b*) loci of the unstable contributing saddle points in the k-plane, for the streamwise long-wave instability (merged S- and H-modes) and for different Galileo numbers G, $\chi = 0$, and $M = 100$. In (*b*), V_r and V_l refer to the right and left boundaries of the unstable ray domains ($Ka = 500$, $Pr = 10$, $L = 0.01$, $B = 0.02$, $\beta = 15°$).

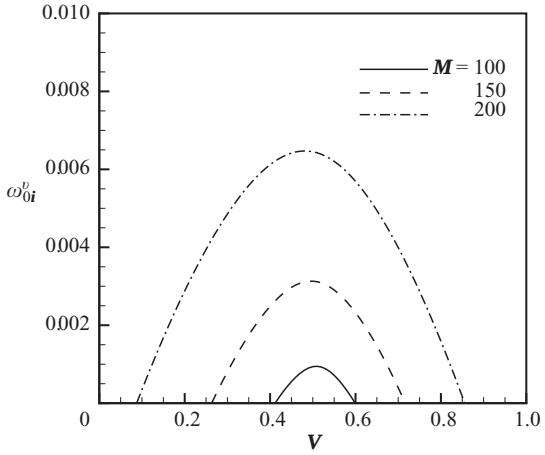

FIGURE 10. Growth rate ω_{0i}^{v} as a function of the ray velocity V for the streamwise long-wave instability (merged S- and H-modes) and for different Marangoni numbers M, $\chi = 0$, and $G = 2$ ($Ka = 500$, $Pr = 10$, $L = 0.01$, $B = 0.02$, $\beta = 15°$).

for different Galileo numbers G in figure 9(*a*). We see that owing to an increased inertial effect, larger Galileo numbers make the flow more unstable in the moving frame with larger downstream velocities. The corresponding loci of the unstable saddle points in the complex k-plane are plotted in figure 9(*b*). From the temporal instability analysis, we know that the long-wave streamwise instability consists of S- and H-modes which merge for large Marangoni or Soret numbers. Moreover, the case chosen here corresponds to a situation where the two modes have already merged (see figure 4*a*). From figure 9(*b*), we learn that a unique group of saddle points, which evolves with the Galileo number, contributes to the spatio-temporal instability of S- and H-modes. This indicates that from the spatio-temporal point of view, the S- and H-modes belong to a single spatio-temporal mode.

For fixed G ($G = 2$), the evolution of ω_{0i}^{v} with V is given for different M ($\chi = 0$) and for different χ ($M = 100$) in figures 10 and 11, respectively. From the two figures,

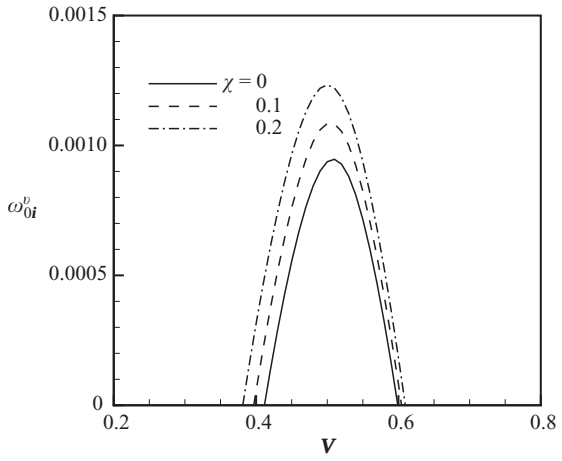

FIGURE 11. Growth rate ω_{0i}^{v} as a function of the ray velocity V for the streamwise long-wave instability (merged S- and H-modes) and for different Soret numbers χ, $M = 100$, and $G = 2$ ($Ka = 500$, $Pr = 10$, $L = 0.01$, $B = 0.02$, $\beta = 15°$).

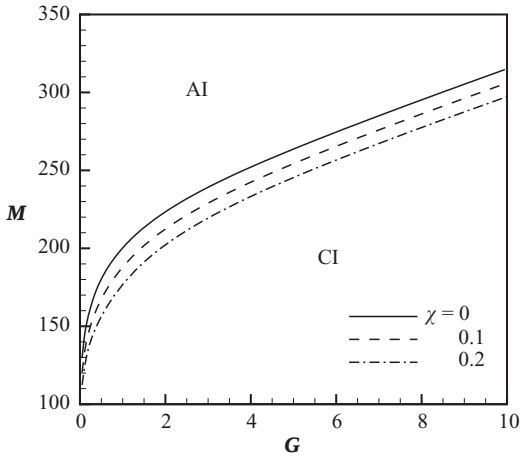

FIGURE 12. AI/CI boundary curves in the M–G parameter space for the streamwise long-wave instability (merged S- and H-modes) and for different Soret numbers χ ($Ka = 500$, $Pr = 10$, $L = 0.01$, $B = 0.02$, $\beta = 15°$).

it is found that larger Marangoni and Soret numbers make the flow more unstable and, at constant inertial effect (constant G), increase the range of unstable rays. A combination of smaller Galileo numbers and larger Marangoni and Soret numbers is thus needed in order to find the zone of absolute instability for this long-wave instability. However, the set of parameters used to plot the curve at $M = 200$ in figure 10 can be used to determine the boundary between absolute and convective instability. The AI/CI boundary curves thus obtained are plotted in the (M, G)-plane for different values of χ in figure 12. It is found that, as expected, larger Marangoni and Soret numbers and smaller Galileo numbers favour the transition to absolute instability. When the Galileo number is small ($G < 2$), the Marangoni number at the AI/CI boundary curve increases very fast with the increase of the Galileo number, while, when the Galileo number is large ($G > 4$), the boundary curve is nearly a

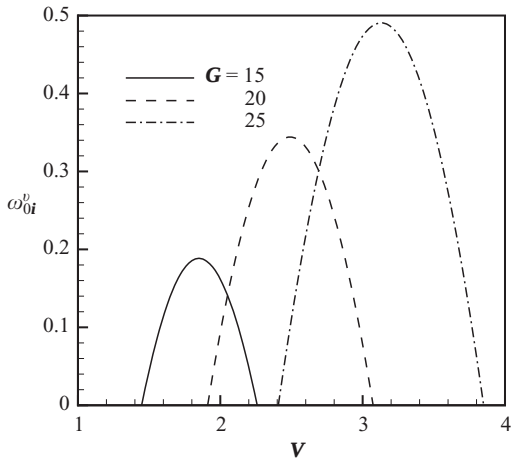

FIGURE 13. Growth rate ω_{0i}^{v} as a function of the ray velocity V for the streamwise short-wave thermocapillary instability (P-mode) and for different Galileo numbers G, $\chi = 0$, and $M = 100$ ($Ka = 500$, $Pr = 10$, $L = 0.01$, $B = 0.02$, $\beta = 15^{\circ}$).

straight line, which means that the Marangoni number is linearly dependent on the Galileo number at the AI/CI transition point in this range of G. In the range chosen ($0 \leqslant \chi \leqslant 0.2$), the influence of the Soret number χ on this AI/CI transition remains moderate and this influence is quite uniform over the whole domain of G.

4.2. *Short-wave spatio-temporal instability of the P-mode*

Concerning the P-modes, the temporal instability analysis has shown that a long-wave instability exists for $\chi > 0$ in the case of spanwise perturbations, but that only a short-wave instability occurs in the case of streamwise perturbations. For this short-wave instability, we perform a similar analysis as in the previous subsection, and thus plot the growth rate ω_{0i}^{v} as a function of the ray velocity V for different Galileo numbers G ($\chi = 0$, $M = 100$), Marangoni numbers M ($\chi = 0$, $G = 15$) and Soret numbers χ ($G = 15$, $M = 100$), respectively in figures 13, 14 and 15. From these figures, we first see that larger Galileo, Marangoni and Soret numbers make the flow more unstable. Moreover, larger Galileo numbers correspond to larger downstream velocities, and larger Marangoni and Soret numbers increase the range of unstable rays. Thus, as for the long-wave instability in the previous subsection, a combination of smaller Galileo numbers and larger Marangoni and Soret numbers is needed to find the zone of absolute instability.

The AI/CI boundary curves obtained for the P-mode are plotted in the (M, G)-plane for different values of χ in figure 16. We see that the increase of the Soret number χ favours the transition to absolute instability. The boundary curves present a local minimum Marangoni number at moderate Galileo number, which decreases as χ is increased. Moreover the behaviour at small Galileo numbers is much changed by the Soret effect: for $\chi = 0$ (without Soret effect), the Marangoni number on the boundary curve goes to infinity as G decreases to zero whereas for $\chi = 0.1$, the Marangoni number reaches a finite value for $G = 0$ and the flow is thus absolutely unstable above this value. Finally, for $\chi = 0.2$, the boundary curve passes through a maximum value before decreasing to a still smaller value at $G = 0$. Note that this value at $G = 0$ is smaller than the local minimum found at finite Galileo numbers.

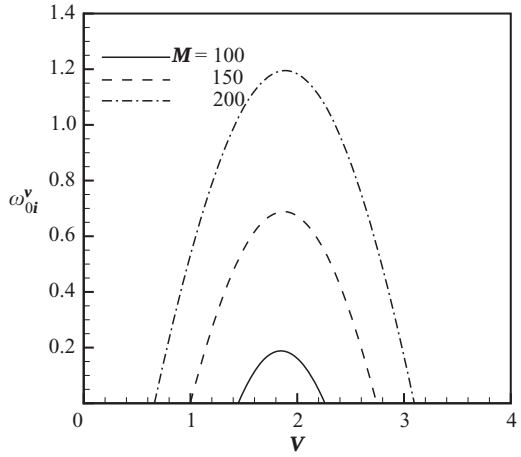

FIGURE 14. Growth rate ω_{0i}^{v} as a function of the ray velocity V for the streamwise short-wave thermocapillary instability (P-mode) and for different Marangoni numbers M, $\chi = 0$, and $G = 15$ ($Ka = 500$, $Pr = 10$, $L = 0.01$, $B = 0.02$, $\beta = 15°$).

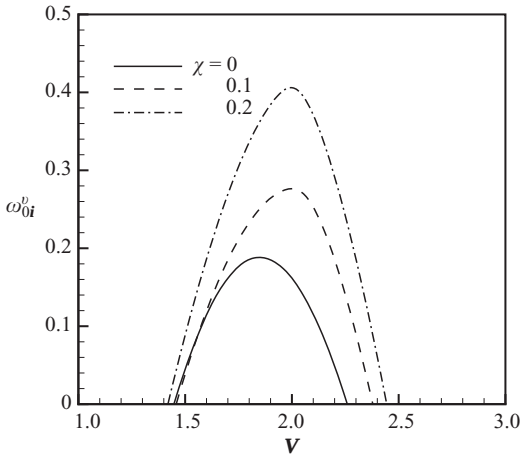

FIGURE 15. Growth rate ω_{0i}^{v} as a function of the ray velocity V for the streamwise short-wave thermocapillary instability (P-mode) and for different Soret numbers χ, $M = 100$, and $G = 15$ ($Ka = 500$, $Pr = 10$, $L = 0.01$, $B = 0.02$, $\beta = 15°$).

4.3. *Critical curves and AI/CI boundary curves for the streamwise instabilities*

The true AI/CI boundary for the streamwise instabilities can only be obtained by considering the boundary curves for both the long-wave and short-wave instabilities. These boundary curves (dotted lines) are plotted together in the (M, G)-plane in figure 17 for two different Soret numbers: $\chi = 0$ and $\chi = 0.1$. We see that, for the two values of χ, the AI/CI boundary curve for the long-wave instability intersects the curve for the short-wave instability. The real AI/CI boundary will thus be determined by the curve (solid line) corresponding to the smallest Marangoni numbers. We see that for small Galileo numbers the AI/CI transition is due to the long-wave instability (S- and H-modes), while for large Galileo numbers it is due to the short-wave instability

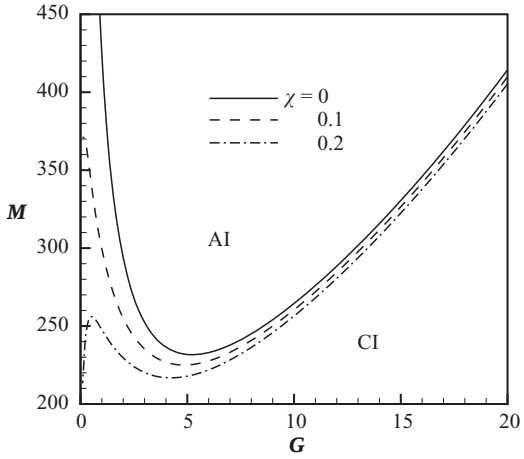

FIGURE 16. AI/CI boundary curves in the M–G parameter space for the streamwise short-wave thermocapillary instability (P-mode) and for different Soret numbers χ ($Ka = 500$, $Pr = 10$, $L = 0.01$, $B = 0.02$, $\beta = 15°$).

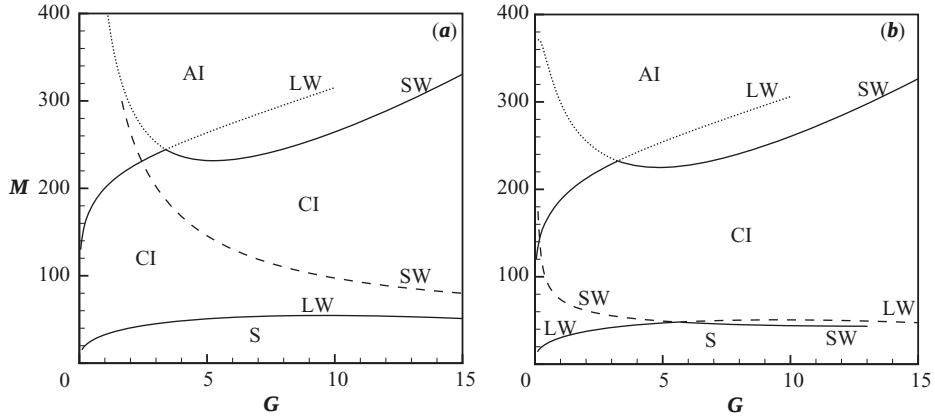

FIGURE 17. AI/CI boundary curves (dotted lines) and critical curves (dashed lines) in the M–G parameter space for both the long-wave (LW) and short-wave (SW) streamwise instabilities: (*a*) $\chi = 0$; (*b*) $\chi = 0.1$. Solid lines are used to indicate the real boundary curves and the real critical curves ($Ka = 500$, $Pr = 10$, $L = 0.01$, $B = 0.02$, $\beta = 15°$).

(P-mode). The critical curves (dashed lines) which show the boundary between the stable and unstable regions are also plotted in the (M, G)-plane in figure 17 for the streamwise instabilities. For $\chi = 0$, i.e. without Soret effect (figure 17*a*), this stable/unstable boundary is determined by the critical curve associated with the long-wave instability. But, for $\chi = 0.1$, owing to the strong influence of χ on the P-mode of instability (figure 4*b*), the critical curve associated with this short-wave instability now intersects the curve associated with the long-wave instability. And the real critical curve (minimum critical Marangoni values, shown as a solid line) indicates that the destabilization of the film is still due to the long-wave instability for small G, but beyond about $G = 6$ is now due to the short-wave instability.

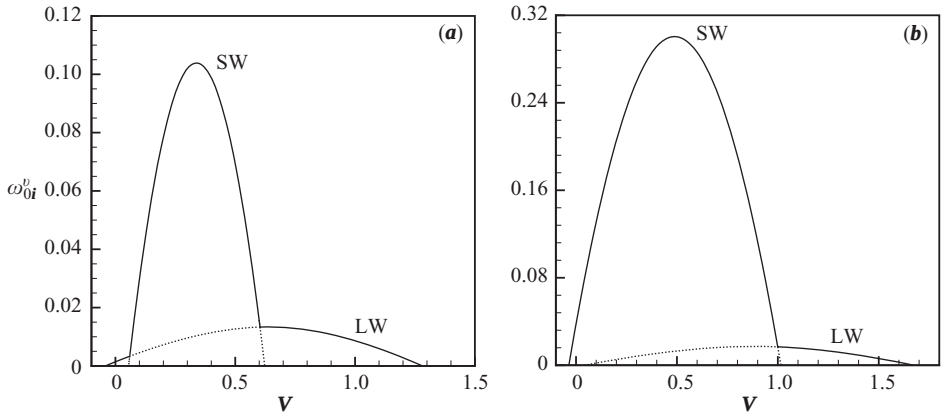

FIGURE 18. Growth rate ω_{0i}^{v} as a function of the ray velocity V for both long-wave (LW) and short-wave (SW) streamwise instabilities and for $\chi = 0$ and $M = 245$: (*a*) $G = 2.8$; (*b*) $G = 4$. The branches of saddle points which determine the properties of the spatio-temporal instability are indicated by solid lines ($Ka = 500$, $Pr = 10$, $L = 0.01$, $B = 0.02$, $\beta = 15^{\circ}$).

4.4. *Saddle-point bifurcations*

In Brevdo *et al.* (1999) on isothermal falling films, a wave packet analysis is conducted based on both the Briggs–Bers collision criterion and the saddle-point approach. This analysis has revealed that, in the case $R(= \rho^2 g h^3 \sin\beta/(2\mu^2)) = 200$ and $\beta = 4.6^{\circ}$, there are bifurcations of the saddle point contributing to the spatio-temporal instability, the ray velocity V being viewed as a bifurcation parameter. Such bifurcations also exist in our problem for parameter values near the intersection of the long-wave and short-wave AI/CI boundary curves. This is shown in figure 18 for two sets of parameters corresponding to $\chi = 0$, $M = 245$ and two values of G, $G = 2.8$ and $G = 4$. In this figure, the growth rates ω_{0i}^{v} of both long-wave and short-wave instabilities are plotted as a function of the ray velocity V. For both values of G, the short-wave instability has a larger maximal growth rate, but occurs in a smaller interval of unstable rays. Moreover, the two unstable saddle-point branches intersect. According to the Briggs–Bers collision criterion (the process is not shown here, but is similar to what is done in Brevdo *et al.* 1999), the properties of the spatio-temporal instability are determined by the branches with the largest local growth rate, and these branches are denoted as solid curves in the figure.

For $G = 2.8$ (figure 18*a*), the two saddle-point branches intersect at two different ray velocities. In this case, on increasing V, two saddle-point bifurcations are found at the left and right boundaries of the unstable ray domain for the short-wave instability, which correspond to a first transition from the unstable long-wave branch to two unstable short-wave and long-wave branches, and then a back transition to the unstable long-wave branch. The intersection points also determine two abrupt changes in the properties of the dominant spatio-temporal instability such as the local oscillatory frequency, spatial amplification rate and spatial wavenumber (change from long-wave to short-wave, and back to long-wave). For $G = 4$ (figure 18*b*), the two saddle-point branches only intersect at one unstable ray velocity, determining one abrupt change in the properties of the dominant spatio-temporal instability (from short-wave to long-wave). In this case, on increasing V, two saddle-point bifurcations are still found, but they are now at the left boundary of the unstable ray domain for the long-wave instability and at the right boundary of the unstable ray domain

for the short-wave instability. For both values of G, the absolute growth rate in the laboratory frame (given by the local growth rate at $V = 0$) is greater than zero, which means that the two situations are absolutely unstable. More precisely, the situation at $G = 2.8$ is absolutely unstable owing to the long-wave instability, whereas the situation at $G = 4$ is absolutely unstable owing to the short-wave instability.

5. Conclusion

In this paper, temporal and spatio-temporal instability analyses have been performed for a binary liquid film with Soret effect flowing down an inclined heated plate. A fixed inclination of the plate ($\beta = 15^\circ$) and fixed values of the Kapitza, Prandtl, Lewis, and Biot numbers (Ka, Pr, L, B) have been chosen, which lead to three variable parameters, the Galileo, Marangoni, and Soret numbers (G, M, χ). Although a Squire transformation exists for this situation, which allows a derivation of the results for any orientation of the perturbation wavenumber from the results obtained for streamwise perturbations, it has been shown that this requires knowledge of the results for all the smaller inclination angles and Galileo numbers. For a fixed inclination angle, this is thus not possible, and we have chosen to derive the stability results for spanwise and streamwise perturbations.

The case of spanwise perturbations in a film on an inclined plate is similar to the perturbations in a horizontal layer where the hydrostatic effect is taken into account, but with an hydrostatic effect proportional to $\cos\beta$ in the case of the inclined film. In this case, we have shown that stationary (oscillatory) thermocapillary S- and P-modes are the most dangerous for positive (negative) Soret numbers χ. Moreover, the P-mode which is short-wave unstable for $\chi = 0$ remains so for $\chi < 0$, but becomes long-wave unstable for $\chi > 0$ and even merges with the long-wave S-mode. This situation is absolutely unstable with respect to the stationary instabilities and convectively unstable with respect to the oscillatory instabilities above the critical values of the parameters.

In the case of streamwise perturbations, it has been shown that larger Soret numbers as well as larger Marangoni numbers make the film flow more unstable. The increase of these parameters leads to the merging of the long-wave surface mode (H-mode) and the long-wave thermocapillary S-mode, so that the situation becomes long-wave unstable for any Galileo number. It also strongly influences the short-wave thermocapillary P-mode which becomes the most critical for enough large Galileo numbers for $\chi = 0.1$. From the spatio-temporal point of view, it is found that the S- and H-modes should belong to the same mode, because the same branch of saddle points contributes to the spatio-temporal local growth of these modes in the moving frame. Thus, there exist two AI/CI boundary curves determined by the long-wave thermocapillary instability of the merged S- and H-modes and by the short-wave thermocapillary instability of the P-mode. The two AI/CI boundary curves in the M–G parameter space intersect each other, and it is found that for small Galileo numbers the AI/CI transition is determined by the long-wave instability, while for large Galileo numbers it is determined by the short-wave instability. Furthermore, this intersection induces a bifurcation of the saddle points contributing to the spatio-temporal instability, similarly to what was found by Brevdo *et al.* (1999) for the isothermal film.

This work was originally funded by a grant from LMFA and IMFT (J. H.). This work is also supported by the National Natural Science Foundation of China (Grants No. 10676005, No. 10676004, No. 10676120 and No. 10702011).

Galileo number	$G = \dfrac{gd^3}{\nu^2}$
Prandtl number	$Pr = \dfrac{\nu}{\kappa}$
Schmidt number	$Sc = \dfrac{\nu}{D}$
Lewis number	$L = \dfrac{D}{\kappa}$
Soret number	$\chi = \dfrac{\alpha\sigma_c}{\sigma_t}$
Marangoni number	$Ma = \dfrac{\sigma_t(T_w - T_a)d}{\mu\kappa}$
Biot number	$Bi = \dfrac{qd}{k_{th}}$
Dimensionless surface tension	$\Sigma = \dfrac{\sigma_0 d}{\rho\nu^2}$
Capillary number	$Ca = \dfrac{\sigma_t(T_w - T_a)}{\sigma_0}$

TABLE 3. Definition of the dimensionless parameters which appear in the governing equations (2.8) and the associated boundary conditions (2.9)–(2.10).

Appendix A. Dimensionless parameters

In the governing equations (2.8) and the corresponding boundary conditions (2.9)–(2.10), there are nine dimensionless parameters which are recalled in table 3, and two relations $L = Pr/Sc$ and $\Sigma\, Ca = Ma/Pr$. Obviously, the Galileo, Marangoni and Biot numbers and the dimensionless surface tension are dependent on the film thickness d. In order that the film thickness only appears in the Galileo number, we adopt the Kapitza number $Ka = \sigma_0/\rho\nu^{4/3}g^{1/3}$ to replace the dimensionless surface tension Σ and define new dimensionless parameters for the Marangoni and Biot numbers:

$$Ka = \Sigma G^{-1/3}, \quad B = Bi\, G^{-1/3}, \quad M = \frac{Ma}{Pr}\, G^{-1/3}. \tag{A 1}$$

Consequently, the relation $\Sigma\, Ca = Ma/Pr$ becomes $Ca = M/Ka$. The new dimensionless system can also be translated into the original one through the three relations:

$$\Sigma = Ka\, G^{1/3}, \quad Bi = B\, G^{1/3}, \quad Ma = M\, Pr\, G^{1/3}. \tag{A 2}$$

Finally, we only need to fix seven independent dimensionless parameters such as the Kapitza, Galileo, Prandtl, Lewis, Soret, Marangoni, and Biot numbers (Ka, G, Pr, L, χ, M, B) as well as the inclination angle (β).

Appendix B. Long-wave approximation (Yih 1963) for the streamwise instabilities

By using $\hat{w} = -\mathrm{i}kf$, $\hat{\theta} = g$, $\hat{c} = h$ and $c = \omega/k$, the linear stability equations (3.1) can be changed to

$$(\mathrm{D}^2 - k^2)^2 f = \mathrm{i}k[(\bar{u} - c)(\mathrm{D}^2 - k^2) - \mathrm{D}^2\bar{u}]f, \tag{B 1a}$$

$$(\mathrm{D}^2 - k^2)g = \mathrm{i}kPr[(\bar{u} - c)g - \mathrm{D}\bar{\theta}\, f], \tag{B 1b}$$

$$(\mathrm{D}^2 - k^2)h + \chi(\mathrm{D}^2 - k^2)g = \mathrm{i}kSc\,[(\bar{u} - c)h - \mathrm{D}\bar{c}\, f]\,, \tag{B 1c}$$

$$f(0) = \mathrm{D}f(0) = g(0) = 0, \tag{B 1d}$$

$$\mathrm{D}h(0) + \chi\,\mathrm{D}g(0) = 0, \tag{B 1e}$$

$$(\mathrm{D}^2 + k^2)f(1) - \frac{\mathrm{D}^2\bar{u}(1)}{\bar{u}(1) - c}f(1) + \mathrm{i}k\frac{Ma}{Pr}[g(1) - h(1)] - \mathrm{i}k\frac{Ma}{Pr}\frac{\mathrm{D}\bar{\theta}(1) - \mathrm{D}\bar{c}(1)}{\bar{u}(1) - c}f(1) = 0, \tag{B 1f}$$

$$[\mathrm{D}^2 - 3k^2 - \mathrm{i}k(\bar{u}(1) - c)]\mathrm{D}f(1) - \frac{\mathrm{i}[\mathrm{D}\bar{p}(1) - \Sigma' k^2]k}{\bar{u}(1) - c}f(1) = 0, \tag{B 1g}$$

$$\mathrm{D}g(1) + Bi\,g(1) - \frac{Bi\,\mathrm{D}\bar{\theta}(1)}{\bar{u}(1) - c}f(1) = 0, \tag{B 1h}$$

$$\mathrm{D}h(1) - \chi Bi\,g(1) + \frac{\chi Bi\,\mathrm{D}\bar{\theta}(1)}{\bar{u}(1) - c}f(1) = 0. \tag{B 1i}$$

The zero-order approximation with respect to the wavenumber k is given by

$$f'''' = 0, \quad g'' = 0, \quad h'' = 0, \tag{B 2a–c}$$

$$f(0) = f'(0) = g(0) = 0, \quad h'(0) + \chi g'(0) = 0, \tag{B 2d, e}$$

$$f''(1) - \frac{\mathrm{D}^2\bar{u}(1)}{\bar{u}(1) - c}f(1) = 0, \quad f'''(1) = 0, \tag{B 2f, g}$$

$$g'(1) + Bi\,g(1) - \frac{Bi\,\mathrm{D}\bar{\theta}(1)}{\bar{u}(1) - c}f(1) = 0, \tag{B 2h}$$

$$h'(1) - \chi Bi\,g(1) + \frac{\chi Bi\,\mathrm{D}\bar{\theta}(1)}{\bar{u}(1) - c}f(1) = 0. \tag{B 2i}$$

The solution of (B 2) can then be expressed as

$$f_0 = z^2, \tag{B 3a}$$

$$g_0 = \frac{Bi}{1 + Bi}\frac{2\mathrm{D}\bar{\theta}(1)}{\mathrm{D}^2\bar{u}(1)}z = \frac{2Bi^2}{(1 + Bi)^2 Re}z, \tag{B 3b}$$

$$h_0 = -\frac{\chi Bi}{1 + Bi}\frac{2\mathrm{D}\bar{\theta}(1)}{\mathrm{D}^2\bar{u}(1)}z + H = -\frac{2\chi Bi^2}{(1 + Bi)^2 Re}z + H, \tag{B 3c}$$

$$c_0 = \bar{u}(1) - \tfrac{1}{2}\mathrm{D}^2\bar{u}(1) = Re, \tag{B 3d}$$

where H will be determined from (B 4c) of the first-order approximation:

$$H = \frac{7}{8}\frac{\chi Bi^2}{(1 + Bi)^2 Re} - \frac{\chi Bi}{2(1 + Bi)Re}.$$

The first-order approximation is then given by

$$f'''' = \mathrm{i}k[(\bar{u} - c_0)f_0'' - \mathrm{D}^2\bar{u}\,f_0], \tag{B 4a}$$

$$g'' = \mathrm{i}kPr[(\bar{u} - c_0)g_0 - \mathrm{D}\bar{\theta}\,f_0], \tag{B 4b}$$

$$h'' + \chi g'' = \mathrm{i}kSc\,[(\bar{u} - c_0)h_0 - \mathrm{D}\bar{c}\,f_0]\,, \tag{B 4c}$$

$$f(0) = f'(0) = g(0) = 0, \tag{B 4d}$$

$$h'(0)+\chi g'(0)=0, \tag{B 4e}$$

$$f''(1)-\frac{\mathrm{D}^2\bar{u}(1)}{\bar{u}(1)-c}f(1)+\mathrm{i}k\frac{Ma}{Pr}[g_0(1)-h_0(1)]-\mathrm{i}k\frac{Ma}{Pr}\frac{\mathrm{D}\bar{\theta}(1)-\mathrm{D}\bar{c}(1)}{\bar{u}(1)-c_0}f_0(1)=0, \tag{B 4f}$$

$$f'''(1)-\mathrm{i}k(\bar{u}(1)-c_0)f_0'(1)-\frac{\mathrm{i}[\mathrm{D}\bar{p}(1)-\Sigma' k^2]k}{\bar{u}(1)-c_0}f_0(1)=0, \tag{B 4g}$$

$$g'(1)+Bi\,g(1)-\frac{Bi\,D\theta(1)}{\bar{u}(1)-c}f(1)=0, \tag{B 4h}$$

$$h'(1)-\chi Big(1)+\frac{\chi BiD\theta(1)}{\bar{u}(1)-c}f(1)=0. \tag{B 4i}$$

If we put $f=f_0+f_1$ and substitute $\bar{u}$, c_0, f_0, g_0 and h_0 into (B 4*a*) and (B 4g), we obtain

$$f_1''''=2\mathrm{i}kRe(z-1), \tag{B 5a}$$

$$f_1'''(1)=\mathrm{i}k\left(2\cot\beta-Re+2\frac{\Sigma'}{Re}k^2\right). \tag{B 5b}$$

From (B 5), we further obtain

$$f_1'''=\mathrm{i}kRe(z-1)^2+\mathrm{i}k\left(2\cot\beta-Re+2\frac{\Sigma'}{Re}k^2\right), \tag{B 6a}$$

$$f_1''=\frac{1}{3}\mathrm{i}kRe(z-1)^3+\mathrm{i}k\left(2\cot\beta-Re+2\frac{\Sigma'}{Re}k^2\right)z+I, \tag{B 6b}$$

$$f_1=\frac{1}{60}\mathrm{i}kRe(z-1)^5+\frac{1}{6}\mathrm{i}k\left(2\cot\beta-Re+2\frac{\Sigma'}{Re}k^2\right)z^3+\frac{I}{2}z^2+Jz+K. \tag{B 6c}$$

From (B 4*d*), we obtain $J=-\frac{1}{12}\mathrm{i}kRe$ and $K=\frac{1}{60}\mathrm{i}kRe$. Equation (B 4*f*) can be written as

$$f_1''(1)-\frac{\mathrm{D}^2\bar{u}(1)}{\bar{u}(1)-c_0}f_1(1)-\frac{\mathrm{D}^2\bar{u}(1)}{(\bar{u}(1)-c)^2}\Delta c f_0(1)+\mathrm{i}k\frac{Ma}{Pr}[g_0(1)-h_0(1)]$$
$$-\mathrm{i}k\frac{Ma}{Pr}\frac{\mathrm{D}\bar{\theta}(1)-\mathrm{D}\bar{c}(1)}{\bar{u}(1)-c_0}f_0(1)=0, \tag{B 7}$$

and, using (B 6), we can deduce that

$$\Delta c=\mathrm{i}k\left[\frac{2}{15}Re^2-\frac{1}{3}Re\cot\beta-\frac{1}{3}\Sigma' k^2+\frac{(3\chi Bi+12\chi+16)Ma\,Bi}{32Pr(1+Bi)^2}\right],$$
$$c=c_0+\Delta c=G\sin\beta$$
$$+\mathrm{i}k\left[\frac{2}{15}(G\sin\beta)^2-\frac{1}{3}G\cos\beta-\frac{1}{3}\Sigma' k^2+\frac{(3\chi Bi+12\chi+16)MaBi}{32Pr(1+Bi)^2}\right].$$

REFERENCES

Benjamin, T. B. 1957 Wave formulation in laminar flow down an inclined plane. *J. Fluid Mech.* **2**, 554–574.

Benney, D. J. 1966 Long waves on liquid films. *J. Math. Phys.* **45**, 150–155.

Bers, A. 1973 Theory of absolute and convective instabilities. In *Survey Lectures, Proceedings of the International Congress on Waves and Instabilities in Plasmas* (ed. G. Auer & F. Cap), pp. B1–B52. Institute for Theoretical Physics, Innsbruck, Austria.

Brevdo, L., Laure, P., Dias, F. & Bridges, T. J. 1999 Linear pulse structure and signalling in a film flow on an inclined plane. *J. Fluid Mech.* **396**, 37–71.

Briggs, R. J. 1964 *Electron-Stream Interaction with Plasmas*. MIT Press.

Canuto, C., Hussaini, M. Y., Quarteroni, A. & Zang, T. A. 1988 *Spectral Methods in Fluid Dynamics*. Springer-Verlag.

Chang, H.-C. 1994 Wave evolution on a falling film. *J. Fluid Mech.* **26**, 103–136.

Deissler, R. J. 1987 Spatially growing waves, intermittency, and convective chaos in an open-flow system. *Physica* D **25**, 233–260.

Gjevik, B. 1970 Occurrence of finite-amplitude surface waves on falling liquid films. *Phys. Fluids* **13**, 1918–1925.

Goussis, D. A. & Kelly, R. E. 1990 On the thermocapillary instabilities in a liquid layer heated from below. *Intl J. Heat Mass Transfer* **33**, 2237–2245.

Goussis, D. A. & Kelly, R. E. 1991 Surface wave and thermocapillary instabilities in a liquid film flow. *J. Fluid Mech.* **223**, 25–45.

de Groot, S. R. & Mazur, P. 1969 *Non-Equilibrium Thermodynamics*. North-Holland.

Hu, J., Ben Hadid, H. & Henry, D. 2007 Linear stability analysis of Poiseuille-Rayleigh-Bénard flows in binary fluids with Soret effect. *Phys. Fluids* **19**, 034101.

Huerre, P. & Monkewitz, P. A. 1985 Absolute and convective instabilities in free shear layers. *J. Fluid Mech.* **159**, 151–168.

Huerre, P. & Monkewitz, P. A. 1990 Local and global instabilities in spatially developing flows. *Annu. Rev. Fluid Mech.* **22**, 473–537.

Joo, S. W. 1995 Marangoni instabilities in liquid mixtures with Soret effects. *J. Fluid Mech.* **293**, 127–145.

Kapitza, P. L. & Kapitza, S. P. 1949 Wave flow of thin layers of a viscous fluid. *Zh. Eksper. Teor. Fiz.* **19**, 105–120, also in Collected Papers of P. L. Kapitza (ed. D. Ter Haar), pp. 690–709. Pergamon, 1965.

Kelly, R. E., Davis, S. H. & Goussis, D. A. 1986 On the instability of heated film flow with variable surface tension. In *Heat Transfer 1986, Proc. 9th Intl Heat Transfer Conference, San Francisco*, vol. 4, pp. 1937–1942. Hemisphere.

Kelly, R. E., Goussis, D. A., Lin, S. P. & Hsu, F. K. 1989 The mechanism for surface wave instability in film flow down an inclined plane. *Phys. Fluids* A **1**, 819–828.

Lin, S. P. 1969 Finite amplitude stability of a parallel flow with a free surface. *J. Fluid Mech.* **36**, 113–126.

Liu, J., Paul, J. D. & Gollub, J. P. 1993 Measurements of the primary instabilities of film flows. *J. Fluid Mech.* **250**, 69–101.

Ooshida, T. 1999 Surface equation of falling film flows with moderate Reynolds number and large but finite Weber number. *Phys. Fluids* **11**, 3247–3269.

Oron, A., Davis, S. H. & Bankoff, S. G. 1997 Long-scale evolution of thin liquid films. *Mod Rev Phys* **69**, 931–980.

Oron, A. & Gottlieb, O. 2002 Nonlinear dynamics of temporally excited falling liquid films. *Phys. Fluids* **14**, 2622–2636.

Pearlstein, A. J. & Goussis, D. A. 1988 Efficient transformation of certain singular polynomial matrix eigenvalue problems. *J. Comput. Phys.* **78**, 305–312.

Pearson, J. R. A. 1958 On convection cells induced by surface tension. *J. Fluid Mech.* **4**, 489–500.

Podolny, A., Oron, A. & Nepomnyashchy, A. A. 2005 Long-wave Marangoni instability in a binary-liquid layer with deformable interface in the presence of Soret effect: Linear theory. *Phys. Fluids* **17**, 104104.

Podolny, A., Oron, A. & Nepomnyashchy, A. A. 2006 Linear and nonlinear theory of long-wave Marangoni instability with the Soret effect at finite Biot numbers. *Phys. Fluids* **18**, 054104.

Pumir, A., Manneville, P. & Pomeau, Y. 1983 On solitary waves running down an inclined plane. *J. Fluid Mech.* **135**, 27–50.

Ruyer-Quil, C. & Manneville, P. 2000 Improved modeling of flows down inclined planes. *Eur. Phys. J.* B **15**, 357–369.

Ruyer-Quil, C. & Manneville, P. 2002 Further accuracy and convergence results on the modeling of flows down inclined planes by weighted-residual approximations. *Phys. Fluids* **14**, 170–183.

Scheid, B., Ruyer-Quil, C., Thiele, U., Kabov, O. A., Legros, J. C. & Colinet, P. 2005 Validity domain of the Benney equation including Marangoni effect for closed and open flows. *J. Fluid Mech.* **527**, 303–335.

Scriven, L. E. & Sternling, C. V. 1964 On cellular convection driven by surface-tension gradients: Effects of mean surface tension and surface viscosity. *J. Fluid Mech.* **19**, 321–340.

Shkadov, V. 1967 Wave flow regimes of a thin layer of viscous fluid subject to gravity. *Isv. Akad. Nauk SSSR* **2**, 43–51.

Smith, K. A. 1966 On convective instability induced by surface-tension gradients. *J. Fluid Mech.* **24**, 401–414.

Sreenivasan, S. & Lin, S. P. 1978 Surface tension driven instability of a liquid film down a heated incline. *Intl J. Heat Mass Transfer* **21**, 1517–1526.

Takashima, M. 1979 Surface tension driven instabillity in a horizontal layer of binary liquid mixture in the presence of the Soret effect. *J. Phys. Soc. Japan* **47**, 1321–1326.

Thiele, U. & Knobloch, E. 2004 Thin liquid films on a slightly inclined heated plate. *Physica* D **190**, 213–248.

Yih, C. S. 1963 Stability of liquid flow down an inclined plane. *Phys. Fluids* **6**, 321–334.

Yin, X.-Y., Sun, D.-J., Wei, M.-J. & Wu, J.-Z. 2000 Absolute and convective instability character of slender viscous vortices. *Phys. Fluids* **12**, 1062–1072.